CHAPTER 10

ULTRAFAST RADIATIONLESS DECAY IN NUCLEIC ACIDS: INSIGHTS FROM NONADIABATIC AB INITIO MOLECULAR DYNAMICS

NIKOS L. DOLTSINIS[1,2*], PHINEUS R. L. MARKWICK[3], HARALD NIEBER[1,2], AND HOLGER LANGER[1]

[1] *Lehrstuhl für Theoretische Chemie, Ruhr-Universität Bochum, 44780 Bochum, Germany*
[2] *Present address: Department of Physics, King's College London, Strand, London WC2R 2LS, United Kingdom*
[3] *Unite de Bioinformatique Structurale, Institut Pasteur, CNRS URA 2185, 25–28 rue du Dr. Roux, 75015 Paris, France*

Abstract: Characterizing the photophysical properties of nucleic acid bases and base pairs presents a major challenge to theoretical modelling. In this Chapter, we focus on the contributions of nonadiabatic ab initio molecular dynamics (na-AIMD) simulations towards unravelling the dynamical mechanisms governing the radiationless decay of DNA and RNA building blocks. The na-AIMD method employed here is based entirely on plane-wave density functional theory and couples nonadiabatically the Kohn-Sham electronic ground state to the restricted open-shell Kohn-Sham first excited singlet state by means of a surface hopping scheme. This approach has been applied to a variety of different nucleobases and tautomers thereof. Gas phase calculations on canonical tautomers serve as a reference to study both substitution and solvation effects. The na-AIMD simulations of nonradiative decay in aqueous solution allow direct comparison with the gas phase results as the same computational setup can be used in both cases. Solute and solvent are both treated explicitly on an equal footing

Keywords: Ab lnitio Molecular Dynamics, Car-Parrinello Molecular Dynamics, Nonadiabatic Effects, Surface Hopping, Excited States, Density Functional Theory, Ultrafast Internal Conversion, Conical Intersections, Nucleobases, Base Pairs, Photostability, UV Genetic Damage

10.1. INTRODUCTION

Nucleic acids exhibit a remarkable robustness with respect to ultraviolet (UV) radiation, which could potentially induce a variety of photochemical reactions

* Corresponding author, e-mail: nikos.doltsinis@kcl.ac.uk

M. K. Shukla, J. Leszczynski (eds.), Radiation Induced Molecular Phenomena in Nucleic Acids, 265–299.

resulting in faulty transscription and thus genetic damage [35]. The mechanism protecting DNA and RNA from suffering UV damage is thought be based on the short lifetime of electronically excited states of nucleic acids [14]. Advances in femtosecond laser spectroscopy [14, 30, 39, 51, 61, 65–69, 71–73, 77, 78, 101, 102] have made possible the systematic study of the photophysical and photochemical properties of individual nucleic acid building blocks, i.e. the purines adenine (A) and guanine (G), and the pyrimidines thymine (T, DNA only), uracil (U, RNA only), and cytosine (C), as well as the GC, AT, and AU base pairs. The structures of the canonical nucleobases and base pairs [7–9, 100] as they occur in DNA and RNA are shown in Figure 10-1. State-of-the-art fluorescence upconversion experiments place the S_1 excited state lifetimes of nucleobases on the sub-picosecond timescale; characteristic decay times as low as 90 fs have been reported [5, 30, 98]. The situation is complicated by the existence of a large number of different tautomers. In the case of G, for instance, at least four tautomeric forms could be distinguished in molecular beam experiments, but spectral assignment proved difficult [10, 31, 43, 53, 61, 67, 77]. In solution, it is assumed that only a single tautomer is present, however the relative stability of G tautomers has been suggested to change in aqueous environment [59, 82].

Nevertheless, it could be demonstrated that the excited state properties of canonical nucleobases and base pairs are decidedly different from those of other forms [44, 45]. In the case of photoexcited DNA base pairs, experimental observations indicate that the canonical, Watson-Crick isomers [7–9, 100] are considerably shorter lived by orders of magnitude than other isomers [2, 79].

From a theoretical point of view, the ultra-short excited state lifetimes observed for canonical structures have been attributed to the existence of easily accessible conical intersections between the excited state and the ground state efficiently promoting nonradiative decay [10, 25, 30, 36, 44, 45, 53, 58, 60, 74, 75, 85, 87, 102]. Accurate prediction of excited state properties still presents a major challenge to

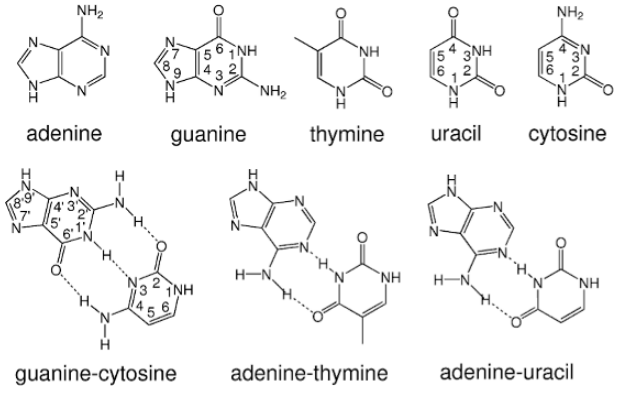

Figure 10-1. Schematic representation of the canonical nucleobases and base pairs

ab initio electronic structure theory, since high-quality calculations are usually not of the 'black box' type, nor are they computationally efficient. The vast majority of quantum chemical studies of nucleobases have therefore been restricted to *static*, single point calculations of excited state energies and the characterization of conical intersections [36, 40, 53, 58, 60, 74–76, 85, 87]. Moreover, these calculations are typically carried out for isolated molecules; solvent effects cannot be taken into account explicitly but only by a polarizable continuum model [30].

In the present chapter, we will focus on the simulation of the *dynamics* of photoexcited nucleobases, in particular on the investigation of radiationless decay dynamics and the determination of associated characteristic time constants. We use a nonadiabatic extension of ab initio molecular dynamics (AIMD) [15, 18, 21, 22] which is formulated entirely within the framework of density functional theory. This approach couples the restricted open-shell Kohn-Sham (ROKS) [26–28] first singlet excited state, S_1, to the Kohn-Sham ground state, S_0, by means of the surface hopping method [15, 18, 94–97]. The current implementation employs a plane-wave basis set in combination with periodic boundary conditions and is therefore ideally suited to condensed phase applications. Hence, in addition to gas phase reference simulations, we will also present nonadiabatic AIMD (na-AIMD) simulations of nucleobases and base pairs in aqueous solution.

10.2. COMPUTATIONAL METHODS

A detailed description of the nonadiabatic AIMD surface hopping method has been published elsewhere [15, 18, 21, 22]; it shall only be summarized briefly here. We have adopted a mixed quantum-classical picture treating the atomic nuclei according to classical mechanics and the electrons quantum-mechanically. In our two-state model, the total electronic wavefunction, Ψ, is represented as a linear combination of the S_0 and S_1 adiabatic state functions, Φ_0 and Φ_1,

$$\Psi(\mathbf{r}, t) = a_0(t)\Phi_0(\mathbf{r}, \mathbf{R}) + a_1(t)\Phi_1(\mathbf{r}, \mathbf{R}) \tag{10-1}$$

where the time-dependent expansion coefficients $a_0(t)$ and $a_1(t)$ are to be determined such that Ψ is a solution to the time-dependent electronic Schrödinger equation,

$$\mathcal{H}(\mathbf{r}, \mathbf{R}(t))\Psi(\mathbf{r}, t) = i\hbar\frac{\partial}{\partial t}\Psi(\mathbf{r}, t) \tag{10-2}$$

$\mathbf{r}$ being the electronic position vector, $\mathbf{R}(t)$ the nuclear trajectory.

In the present case, our adiabatic basis functions are the S_0 closed-shell Kohn-Sham ground state determinant,

$$\Phi_0 = |\phi_1^{(0)}\bar{\phi}_1^{(0)}\cdots\phi_n^{(0)}\bar{\phi}_n^{(0)}\rangle \tag{10-3}$$

and the orthonormalized S_1 wavefunction

$$\Phi_1 = \frac{1}{\sqrt{1-S^2}}\left[-S\Phi_0 + \Phi_1'\right] \tag{10-4}$$

where

$$S = \langle \Phi_0 | \Phi_1' \rangle \tag{10-5}$$

is the overlap between the ground state wavefunction and the ROKS excited state wavefunction [26–28]

$$\Phi_1' = \frac{1}{\sqrt{2}}\left\{ |\phi_1^{(1)}\bar{\phi}_1^{(1)}\cdots\phi_n^{(1)}\bar{\phi}_{n+1}^{(1)}\rangle + |\phi_1^{(1)}\bar{\phi}_1^{(1)}\cdots\bar{\phi}_n^{(1)}\phi_{n+1}^{(1)}\rangle \right\} \tag{10-6}$$

n being half the (even) number of electrons. Separate variational optimization of Φ_0 and Φ_1' generally results in nonorthogonality, the molecular orbitals $\phi_l^{(0)}$ and $\phi_l^{(1)}$ are different. Please note, however, that for small S, $\Phi_1 \approx \Phi_1'$.

Substitution of ansatz (10-1) into (10-2) and integration over the electronic coordinates following multiplication by Φ_k^* $(k = 0, 1)$ from the left yields the coupled equations of motion for the wavefunction coefficients

$$\dot{a}_k(t) = -\frac{i}{\hbar}a_k(t)E_k - \sum_l a_l(t)D_{kl} \quad (k, l = 0, 1) \tag{10-7}$$

where E_k is the energy eigenvalue associated with the wavefunction Φ_k. For the nonadiabatic coupling matrix elements

$$D_{kl} = \langle \Phi_k | \frac{\partial}{\partial t} | \Phi_l \rangle \tag{10-8}$$

the relations $D_{kk} = 0$ and $D_{kl} = -D_{lk}$ hold, as our Φ_k are real and orthonormal.

In the Car-Parrinello molecular dynamics (CP-MD) formalism [6, 57], computation of the nonadiabatic coupling elements, D_{kl}, is straightforward and efficient, since the orbital velocities, $\dot{\phi}_l$, are available at no additional cost due to the underlying dynamical propagation scheme. If, instead of being dynamically propagated, the wavefunctions are optimized at each point of the trajectory (so-called Born-Oppenheimer mode), the nonadiabatic coupling elements are calculated using a finite difference scheme.

Numerical integration of (10-7) yields the expansion coefficients a_k, whose square moduli, $|a_0|^2$ and $|a_1|^2$, can be interpreted as the occupation numbers of ground and excited state, respectively.

Following Tully's *fewest switches criterion* [94] recipe, the nonadiabatic transition probability from state k to state l is

$$\Pi_{kl} = \max(0, P_{kl}) \tag{10-9}$$

with the transition parameter

$$P_{kl} = -\delta t \, \frac{\frac{d}{dt}|a_k|^2}{|a_k|^2} \tag{10-10}$$

where δt is the MD time step.

A hop from surface k to surface l is carried out when a uniform random number $\zeta > \Pi_{kl}$ provided that the potential energy E_l is smaller than the total energy of the system. The latter condition rules out any so-called classically forbidden transitions. After each surface jump atomic velocities are rescaled in order to conserve total energy. In the case of a classically forbidden transition, we retain the nuclear velocities, since this procedure has been demonstrated to be more accurate than alternative suggestions [63] .

The two-state surface hopping formalism presented here can be easily generalized to include multiple excited states [94]. However, calculating a large number of electronic states including nonadiabatic couplings between them from first principles is often either not straightforward or too computationally demanding in practice. Our two-state approach can present a severe limitation in cases where at least three electronic states are required to capture the system's chemistry or physics. In some of the applications discussed below, however, we implicitly take into account more than two electronic states because the character of the S_1 wavefunction changes adiabatically as the nuclei move along the trajectory.

In the studies presented in this chapter, excited state nonradiative lifetimes, τ, have been determined by fitting either a mono-exponential function

$$N(t) = N_0 e^{-t/\tau} \tag{10-11}$$

or a bi-exponential function

$$N(t) = c e^{-t/\tau_1} + (N_0 - c) e^{-t/\tau_2} \tag{10-12}$$

where N_0 is the number of trajectories. Equations (10-11) and (10-12) satisfy the boundary condition that at time $t = 0$ all molecules are in the S_1 state.

An alternative way of estimating the excited state lifetime is to compute the ratio of the MD timestep, δt and the ensemble and time averaged transition probability $< \Pi_{10} >$,

$$\tau = \delta t / < \Pi_{10} > \tag{10-13}$$

Here we exploit the observation that once a hop to the ground state has occured transitions back to the excited state are extremely rare for the systems investigated.

All na-AIMD calculations reported in this chapter have been performed using the `CPMD` package [1] employing the BLYP exchange-correlation functional [3, 48] and a plane-wave basis set truncated at 70 Ry in conjunction with Troullier-Martins pseudopotentials [93]. For further details we refer the reader to the respective original articles.

10.3. RESULTS AND DISCUSSION

10.3.1. Uracil

10.3.1.1. Gas phase reference calculations

10.3.1.1.1. Excited state potential and conical intersections To this end, we discuss the excitation energies to the lowest lying $\pi\pi^*$ state at ground and excited state optimized geometries. Table 10-1 summarizes our gas phase ROKS results [64] for vertical excitation energies, ϵ^{vert}, adiabatic excitation energies, ϵ^{adiab}, and fluorescence energies, ϵ^{fluor}, and compares them to other nucleobases.

It is well known that ROKS systematically underestimates excitation energies, this has also been reported for other nucleobases [43–45, 47, 56]. Typically, however, the shape of the ROKS potential landscape, which determines the excited state dynamics, has been found to be surprisingly accurate [16, 20, 21, 56]. An indication for this are the Stokes shifts obtained with ROKS. The experimental Stokes shift of 0.91 eV measured in aqueous solution [30] is much smaller than the gas phase ROKS results (Table 10-1). TDDFT calculations taking into account solvent effects through a polarizable continuum model seem to confirm that the Stokes shift is significantly reduced (by 0.4 eV) due to the solvent [30]. Nieber and Doltsinis [64] have calculated the Stokes shift in explicit water solvent using ROKS/DFT; we shall discuss these condensed phase simulations in detail below (see Section 10.3.1.2).

Moreover, Nieber and Doltsinis [64] have studied the effect of thermal molecular motion on the fluorescence energy by averaging over 10 configurations sampled from a 300 K ROKS S_1 CP-MD run. Due to the flatness of the ROKS S_1 PES, the

Table 10-1. Calculated excited state properties of nucleobases and base pairs. Vertical excitation energy, $\varepsilon^{\text{vert}}$, relative excited state energies, ε^{rel}, adiabatic excitation energies, $\varepsilon^{\text{adiab}}$, fluorescence energies, $\varepsilon^{\text{fluor}}$, Stokes shifts, $\varepsilon^{\text{Stokes}}$, relaxation energies, $\varepsilon^{\text{relax}} = \varepsilon^{\text{vert}} - \varepsilon^{\text{adiab}}$, in eV, and root mean square distances relative to the S_0 global minimum, RMSD, in Å. Excited state nonradiative lifetimes, τ, are given in ps. The results for U(300 K) and U(aq) are thermal averages in the gas phase and in liquid water, respectively

structure	$\varepsilon^{\text{vert}}$	ε^{rel}	$\varepsilon^{\text{adiab}}$	$\varepsilon^{\text{fluor}}$	$\varepsilon^{\text{Stokes}}$	$\varepsilon^{\text{relax}}$	RMSD	τ
U	3.58	–	3.09	1.73	1.85	0.49	0.15	0.6
U(300 K)	3.48	–	–	2.04	1.44	–	–	0.6
U(aq)	3.56	–	–	2.10	1.46	–	–	0.4
C	3.30	–	2.78	1.73	1.57	0.53	0.13	0.7
C [Me]	3.68	–	3.16	1.83	1.85	0.52	0.13	0.5
G [9H-keto-a]	3.70	0.29	3.37	2.45	1.25	0.34	0.07	0.8
G [9H-keto-b]	3.70	0.03	3.11	1.97	1.73	0.59	0.11	0.8
G [9H-keto-c]	3.70	0.00	3.08	1.75	1.95	0.62	0.24	0.8
G(aq) [9H-keto]	3.55	–	–	–	–	–	–	2.0
G [9Me-keto-c]	3.69	0.00	3.05	1.72	1.97	0.64	0.23	1.3
G [7H-keto-a]	3.34	0.00	2.87	2.56	0.78	0.47	0.06	1.0
G [7Me-keto-a]	3.39	0.00	2.89	2.47	0.92	0.50	0.05	1.7
GC	3.42	–	2.60	0.94	2.48	0.82	0.07	0.03/0.3
GC(aq)	3.61	–	2.50	0.75	2.86	1.11	–	0.03/0.3

thermal shift on ϵ^{fluor} is rather large, resulting in an increase of ϵ^{fluor} by 0.31 eV. These findings suggest that it is important to take into account thermal fluctuations in order to be able to reproduce the experimental Stokes shift.

The TDDFT/BLYP vertical excitation energy of 4.72 eV computed by Nieber and Doltsinis [64] is in good agreement with the experimental value of 4.79 eV [30], while the TDDFT/PBE0 results of 5.26 eV by Gustavsson et al. [30] slightly overestimates ϵ^{vert}. The fact that the very sophisticated MRCI calculation by Matsika [58] yields a value for ϵ^{vert} which overshoots by more than 1 eV demonstrates the challenging nature of the excited state electronic structure problem. CASPT2 calculations yield $\epsilon^{\text{vert}} = 5.00$ eV [50] close to the experimental number, while the DFT/MRCI result of 5.44 eV by Marian et al. [54] is somewhat too high.

The most notable structural changes upon geometry optimization in the S_1 state using ROKS are the elongation of the $C^{(5)}C^{(6)}$ bond by 0.14 Å and the increase of the $H^{(5)}C^{(5)}C^{(6)}H^{(6)}$ dihedral angle, θ, by 60°. This is consistent with previous calculations on uridine [17]. A graphical representation of the ground state and S_1 excited state optimized structures is shown in Figure 10-2 together with the ROKS singly occupied molecular orbitals (SOMOs) for vertically excited uracil as well as for the S_1 minimum. They clearly show that the $\pi\pi^*$ character of the electronic excitation is preserved upon excited state geometry optimization. Excited state AIMD simulations of uridine [17] also suggest that the $H^{(5)}C^{(5)}C^{(6)}H^{(6)}$ dihedral angle is the primary parameter determining the value of the $S_0 - S_1$ energy gap. In other words, increasing θ is expected to lead to a conical intersection. In order to verify this hypothesis a series of constrained geometry optimizations in the S_1 state at fixed values of θ has been carried out. The S_0 and S_1 energies along this path are shown in Figure 10-3. The closed shell ground and ROKS excited states cross at $\theta \approx 110°$. In CASSCF [30] and MRCI [58] studies conical intersections were characterized by strong pyramidalization of the $C^{(5)}$ atom, the CASSCF structure having a dihedral angle of $\theta = 118°$. Thus the ROKS potential energy surfaces appear to be able to reproduce the most important features observed in higher level

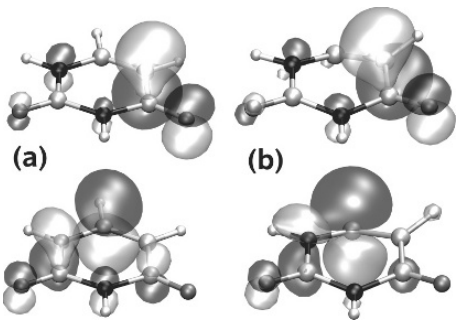

Figure 10-2. Singly occupied molecular orbitals of uracil obtained with the ROKS method for vertical excitation (a) and at S_1 optimized geometry (b). H atoms are shown in *white*, C atoms in *light grey*, O atoms in *dark grey*, and N atoms in *black*

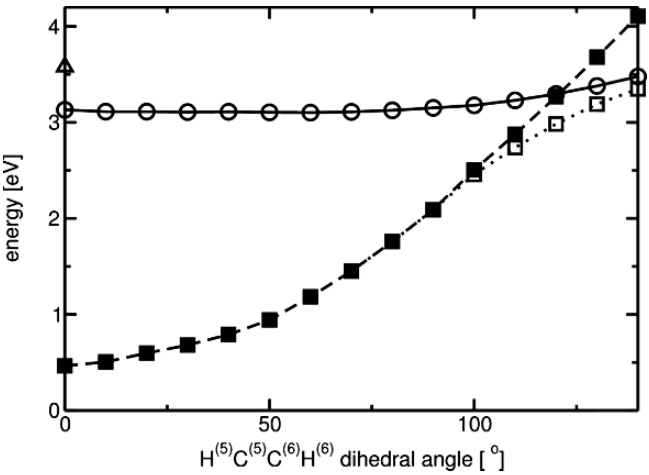

Figure 10-3. ROKS (*solid line, open circles*) S_1 energies and spin-restricted (*dashed line, filled squares*) and spin-unrestricted (*dotted line, open squares*) ground state energies calculated at constraint optimized ROKS S_1 geometries of uracil for fixed values of the $H^{(5)}C^{(5)}C^{(6)}H^{(6)}$ dihedral angle. The vertical excitation energy at a dihedral angle of 0° is represented by a triangle. All energies are given relative to the ground state minimum

quantum chemical single point studies. Therefore they represent a suitable basis for performing nonadiabatic molecular dynamics simulations.

10.3.1.1.2. Nonradiative decay dynamics In a first series of simulations, 30 nonadiabatic surface hopping trajectories were calculated starting from different initial configurations sampled at random from a ground state CP-MD run at 300 K. At the moment of vertical excitation the temperature in the S_1 state is thus $T_i = 300$ K; the molecules subsequently pick up kinetic energy as they fall into the S_1 global potential minimum and approach the conical intersection region where nonadiabatic transitions back to the ground state occur.

For the ensemble of 30 surface hopping trajectories, Figure 10-4 shows the S_1 excited state population as a function of time, t, after photoexcitation. Fitting a mono-exponential function (10-11) to the S_1 population subject to the boundary condition that all molecules are in the S_1 state at $t = 0$ a nonradiative decay time of 608 fs at $T_i = 300$ K has been determined. Gas phase measurements [5, 98] of uracil suggest the existence of a bi-exponential decay mechanism, the time constants for the rapid and the slow channel being 50–100 fs and 0.5–1.0 ps, respectively. Thus the theoretical lifetime from na-AIMD at an initial temperature of $T = 0$ K is of the same order of magnitude as the slow decay component determined in the most recent experimental results. It has been argued that a nonadiabatic transition from the initially populated bright $\pi\pi^*$ state to an optically dark $n\pi^*$ state is responsible for the fast component, while the transition from the $n\pi^*$ state to the ground state occurs on the slower timescale [13, 14, 30, 102].

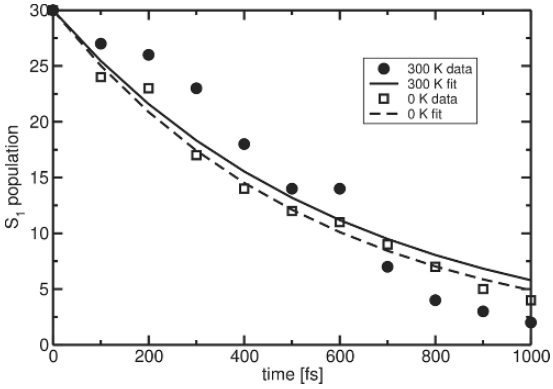

Figure 10-4. S_1 population of uracil as a function of time after vertical excitation for an ensemble of 30 trajectories initialized in the S_1 state at $T_i = 300\ K$ (•) and with zero kinetic energy ($T_i = 0$ K, □). Mono-exponential fits yield S_1 lifetimes of 608 ± 67 fs (300 K) and 551 ± 17 fs (0 K), respectively

In view of the relatively small number of trajectories that Nieber and Doltsinis [64] have been able to calculate within the na-AIMD approach, a bi-exponential fit is inappropriate. However, their result derived from the mono-exponential fit may represent an average over the experimentally determined slow and fast components. It is worth emphasizing that according to the na-AIMD simulations such a sub-picosecond relaxation can be explained purely in terms of coupled $\pi\pi^*$ excited state/ground state dynamics without the involvement of any other electronic states. The sub-100 fs decay component measured experimentally may be connected to the large intial geometric changes associated with moving from the Franck–Condon region to the excited state global minimum.

In order to study the effect of the initial S_1 vibrational temperature, T_i, on the nonradiative lifetime, 30 additional surface hopping trajectories have been carried out setting all velocities to zero at the moment of vertical excitation, i.e. $T_i = 0$ K. The corresponding S_1 population as a function of time is plotted in Figure 10-4. Again a mono-exponential fit was performed, yielding a lifetime of 551 fs. Thus there is no significant difference between the results for $T_i = 0$ K and $T_i = 300$ K. This finding may hint at the fact experimental nonradiative decay times are rather insensitive to the amount of excess energy deposited in the molecule, contrary to previous suggestions [14].

Going beyond the determination of excited state lifetimes, in the following we shall present a detailed analysis of the mechanism of radiationless decay. For this purpose we compare the time evolution of certain geometric parameters such as bond lengths, bond angles, and dihedral angles to the time-dependence of the $S_0 - S_1$ energy gap, ϵ, and the nonadiabatic surface hopping transition parameter, P_{10}. The latter is used in the fewest switches surface hopping scheme [18, 22, 94] to calculate the probability for a jump from S_1 to S_0.

Figure 10-5 shows a comparison of the energy gap with the $C^{(5)}C^{(6)}$ bond length and the $H^{(5)}C^{(5)}C^{(6)}H^{(6)}$ dihedral angle as a function of time. The latter is seen to

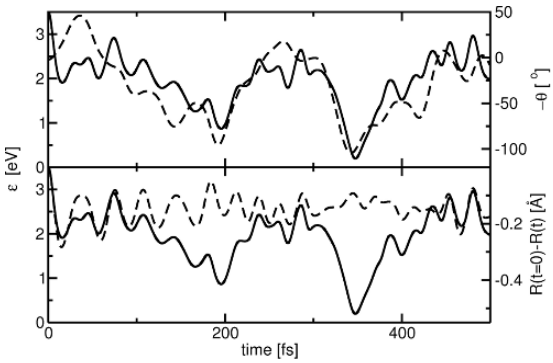

Figure 10-5. Comparison of the time evolution of the $S_0 - S_1$ energy gap, ϵ (*solid line*), with that of the $H^{(5)}C^{(5)}C^{(6)}H^{(6)}$ dihedral angle (*upper panel, dashed line*) and the $C^{(5)}C^{(6)}$ bond length (*lower panel, dashed line*) of uracil

describe the overall shape, that is the low frequency fluctuations, of the ϵ curve very well. Its high frequency modulation, on the other hand, agrees well with the $C^{(5)}C^{(6)}$ bond vibrations. Therefore, these two coordinates appear to be sufficient to model variations in the energy gap. This information could be used in subsequent studies to construct a low-dimensional potential energy surface using highly accurate ab initio quantum chemical methods.

The upper panel of Figure 10-6 illustrates the correlation between the nonadiabatic surface hopping parameter P_{10} and changes in the $C^{(5)}C^{(6)}$ bond length. In other words, vibrations of the $C^{(5)}C^{(6)}$ bond are seen to modulate the nonadiabatic transition probability. This confirms the above finding (Figure 10-5) which links changes in the energy gap to changes in the $C^{(5)}C^{(6)}$ bond length.

Moving on to other geometric variables, the $C^{(2)}N^{(1)}C^{(5)}C^{(4)}$ dihedral angle is seen to describe well, on a slower time scale, the envelope of P_{10} (middle panel of Figure 10-6). This geometric parameter describes out-of-plane distortions of the six-membered ring which are predominantly induced by the pyramidalization of the $C^{(5)}$ atom. Molecular motion of this type has been recognized previously [30, 40, 58] to be responsible for nonradiative decay.

Interestingly, the time-derivative of the $S_0 - S_1$ energy gap also exhibits good correlation with P_{10} (Figure 10-6, bottom panel). This is particularly noteworthy as in the literature the energy gap itself is frequently assumed to be a good parameter to estimate the transition probability. The nonadiabatic simulations clearly demonstrate that this is not the case.

10.3.1.2. Uracil in aqueous solution

In order to study solvent effects on the excited state photophysical properties and nonradiative decay of uracil, additional na-AIMD simulations of uracil in liquid water have been carried out [64]. Figure 10-7 shows the periodic simulation cell containing uracil and 39 water molecules. We have verified that at any time in

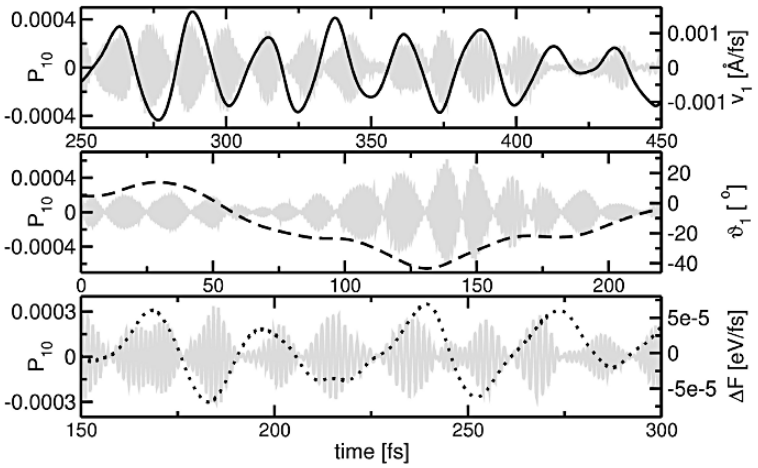

Figure 10-6. Comparison of the time-dependent nonadiabatic hopping parameter, P_{10} (*grey lines*), with the time derivative of the $C^{(5)}C^{(6)}$ bond (v_1, *upper panel, solid black line*), the dihedral angle $C^{(2)}N^{(1)}C^{(5)}C^{(4)}$ (ϑ_1, *middle panel, dashed black line*), and the time derivative of the $S_0 - S_1$ energy gap (ΔF, *bottom panel, dotted black line*) for selected pieces of a typical uracil trajectories

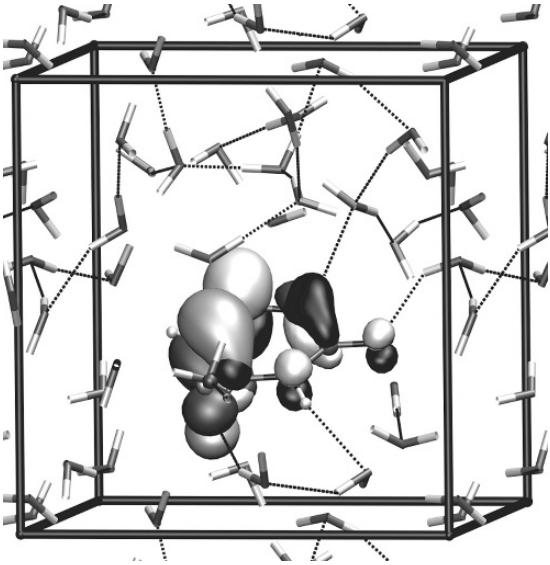

Figure 10-7. Periodically repeated simulation unit cell containing uracil and 39 water molecules. The SOMOs of the ROKS $\pi\pi^*$ excited state are shown in *dark grey/light grey* and *black/white*

between photoexcitation and relaxation to the ground state, the system remains in a $\pi\pi^*$ excited state localized on the uracil molecule (see Figure 10-7 for a graphical representation of the SOMOs). Let us first discuss the effect of the water solvent on excitation and de-excitation energies. Comparison of the thermally averaged vertical excitation energies in the gas phase and in solution reveals that the value in solution is only marginally larger by 0.1 eV (see Table 10-1). However, the statistical error on ϵ^{vert} is $\pm$ 0.2 eV. Also the vertical de-excitation (fluorescence) energy in solution is close to the gas phase finite temperature value, the statistical errors being $\pm$ 0.5 eV and $\pm$ 0.4 eV in gas phase and solution, respectively. Thus a Stokes shift in solution of $1.46 \pm$ 0.63 eV is obtained (Table 10-1), in fair agreement with the experimental value of 0.91 eV [30]. Unfortunately, due to the large statistical uncertainties any small differences between the gas phase and the aqueous solution could not be resolved.

Regarding solvent effects on the uracil structure, a comparison of optimized geometries is not meaningful, since there are numerous nearly degenerate local minima in solution. We therefore compare thermal distributions of geometric variables. The most significant change in solution concerns the $H^{(5)}C^{(5)}C^{(6)}H^{(6)}$ whose excited state distribution is seen to be much narrower in solution (Figure 10-8). The histogram in the condensed phase has its biggest peak around 0° whereas the gas phase histogram shows two peaks near the S_1 minimum around $\pm$ 60°.

Nieber and Doltsinis [64] calculated 15 nonadiabatic surface hopping trajectories starting from configurations and velocities sampled from a ground state simulation. The nonradiative excited state lifetime has been determined by fitting the time-dependent, decaying excited state ensemble population to a mono-exponential function subject to the boundary condition that all molecules were in the S_1 state

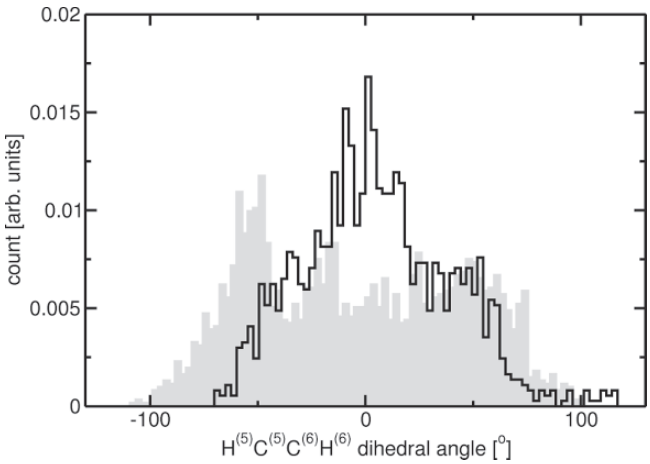

Figure 10-8. Normalized distributions of the $H^{(5)}C^{(5)}C^{(6)}H^{(6)}$ dihedral angle from excited state thermally equilibrated AIMD simulations of uracil in the gas phase (*grey*) and in aqueous solution (*black*)

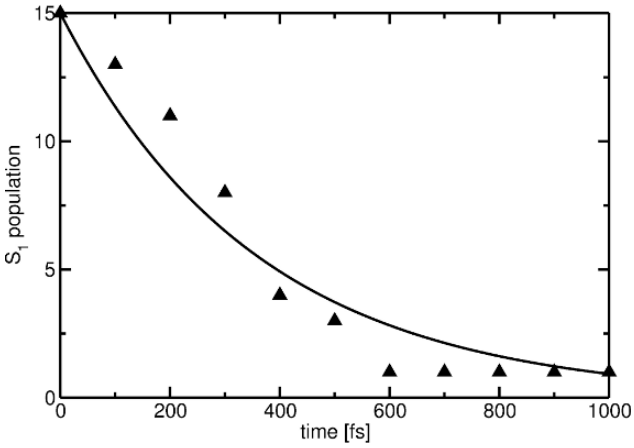

Figure 10-9. S_1 population (▲) as a function of time after vertical excitation for an ensemble of 15 trajectories of uracil in aqueous solution initialized in the S_1 state at a vibrational temperature of $T = 350$ K. A monoexponential fit (*solid line*) yields a S_1 lifetime of 359 ± 34 fs

at time $t = 0$ (see Figure 10-9). Thus a lifetime of 359 fs is obtained, slightly shorter than the gas phase na-AIMD result at room temperature. However, due to the smaller number of trajectories in solution, the statistical uncertainty is higher than for the gas phase. In general, solvent effects on S_1 lifetimes have been found to be rather small [14]. Very recently Gustavsson et al. [30] measured a fluorescence decay time of 96 ± 3 fs (experimental uncertainty 100 fs) using femtosecond fluorescence upconversion. Using the Strickler-Berg relation [90] they arrive at a fluorescence lifetime of 250 fs. Kohler and co-workers determined a S_1 lifetime of 210 fs for uridine in aqueous solution using transient absorption spectroscopy [13]. The theoretical na-AIMD results are thus in fairly good agreement with experiment.

Analogously to the analysis presented in Section 10.3.1.1.2 for the gas phase, Nieber and Doltsinis [64] have attempted to establish possible correlations between the time-dependent surface hopping parameter, P_{10}, and certain geometric variables as well as the $S_0 - S_1$ energy gap. The hopping parameter P_{10} appears to be modulated by variations in the $C^{(5)}C^{(6)}$ and $C^{(4)}C^{(5)}$ bond lengths. Moreover, the oscillations in the time derivative of the $S_0 - S_1$ energy gap are seen to match well those of P_{10}. Hence, there does not seem to be any qualitative difference in the mechanism of nonradiative decay in solution compared to the gas phase.

10.3.2. Cytosine

10.3.2.1. H-keto C

The photophysical properties of cytosine are very similar to those of uracil (Section 10.3.1). The global $\pi\pi^*$ excited state minimum structure is characterized by a large $H^{(5)}C^{(5)}C^{(6)}H^{(6)}$ dihedral angle of 66° [41, 42] and a $C^{(5)}C^{(6)}$ bond length

of 1.48 Å, elongated by 0.1 Å with respect to the ground state geometry. In analogy to uracil (see Figure 10-3), Langer and Doltsinis have calculated a cut through the excited state and ground state PESs along the $H^{(5)}C^{(5)}C^{(6)}H^{(6)}$ dihedral angle for C. They observe a state crossing at 147°. This value is larger than the result reported for uracil because in there the structures were allowed to relax in the S_1 state. Conical intersections between the $\pi\pi^*$ excited state and the ground state have also been found by Merchán and Serrano-Andrés [60], Tomić et al. [92], and Kistler and Matsika [40].

Nonradiative decay of C has been studied by calculating an ensemble of 16 nonadiabatic AIMD trajectories [41, 42]. A mono-exponential fit to the decaying excited state population yields the lifetime of 0.7 ps, while the relation (10-13) leads to the interval [0.4…0.7…2.7] ps. Thus the calculated lifetime is inbetween the lifetimes of U and 9H-keto G. Kang et al. [37] experimentally determined a lifetime of 3.2 ps, while Canuel et al. [5] observe a bi-exponential decay with the time constants 160 fs and 1.86 ps. Ullrich et al. [98] measure the lifetimes < 50 fs, 820 fs, and 3.2 ps using time-resolved photoelectron spectroscopy, their assignment to different electronic states is however unclear.

Langer and Doltsinis [41, 42] find that the nonadiabatic transition parameter (10-10) is correlated to variations in the $C^{(5)}C^{(6)}$ bond length as well as to out-of-plane motions. The importance of this degree of freedom for radiationless decay has been pointed out previously by Zgierski et al. [103].

10.3.2.2. Me-keto C

Substitution of hydrogen $H^{(1)}$ by a methyl group has been found to have a significant impact on the excited electronic state of C, in contrast to the observations for G (see Sections 10.3.3.2.3 and 10.3.3.2.4). In the case of Me-keto C, the ROKS method does not describe the bright $\pi\pi^*$ state but a dark $n\pi^*$ state [41, 42]. Stabilization of a dark state by methylation has also been suggested by the REMPI spectrocopic measurements of He et al. [34]. The optimized S_1 structure closely resembles the $\pi\pi^*$ structure of the unmethylated species. However, the vertical and adiabatic excitation energies of Me-keto C are higher by 0.4 eV compared to H-keto C (see Table 10-1).

Again, 16 AIMD surface hopping simulations were carried out to study the internal conversion process of Me-keto C [41, 42]. Using the mono-exponential fitting procedure (10-11) an excited state lifetime of 0.5 ps is obtained. Employing the average transition probability (10-13) results in the interval [0.4…0.7…3.5] ps. Comparison of the mono-exponential fits for Me-keto C and H-keto C suggests that methylation slightly shortens the excited state lifetime, unlike in the case of G (see Table 10-1). However, we should bear in mind that for Me-keto C the simulation proceeds in the dark $n\pi^*$ state, whereas the $\pi\pi^*$ state determines the dynamics in all other cases described in this article.

Experimental results for Me-keto G are not known, but the derivatives Cyd and dCMP have been investigated in solution. For Cyd the excited state lifetime was determined to be 720 fs by Percourt et al. [73] and 1.0 ps by Malone et al. [52]. In the

case of dCMP, Onidas et al. [70] obtained 530 fs assuming mono-exponential decay, and 270 fs and 1.4 ps assuming bi-exponential decay. On the whole, therefore, the theoretical results of Langer and Doltsinis [41, 42] are in good agreement with the experimental results available.

10.3.3. Guanine

10.3.3.1. Tautomerism

10.3.3.1.1. Gas phase Ground state DFT and excited state ROKS calculations using the BLYP functional by Langer and Doltsinis [43] suggest that 7H-keto G is the most stable tautomer both in the ground state and in the first excited $\pi\pi^*$ state, slightly lower in energy than the 9H-keto tautomer. The ground state structures of the six most stable tautomers are depicted in Figure 10-10.

Upon excitation to the S_1 state, substantial geometrical distortions have been observed in particular for the biologically relevant, canonical 9H-keto tautomer whose six-membered aromatic ring is heavily nonplanar. The calculated adiabatic S_1 excitation energies can be compared to experimental 0–0 transition energies providing hints as to the spectral positions of the individual G tautomers. In combination with the ROKS S_1 vibrational spectra, the theoretical results facilitate the assignment of experimental IR-UV and REMPI spectra of jet-cooled G [61, 67, 77]. A number of recent studies have tackled the issue of G tautomerism [10, 53, 62] suggesting the existence of rare tautomers in supersonic jets.

Langer and Doltsinis [43] have demonstrated that excited state vibrational frequencies can be obtained fairly reliably using the ROKS method. In particular, unlike the more conventional CIS and CASSCF methods, ROKS does not require any rescaling of vibrational frequencies. Velocity autocorrelation functions obtained

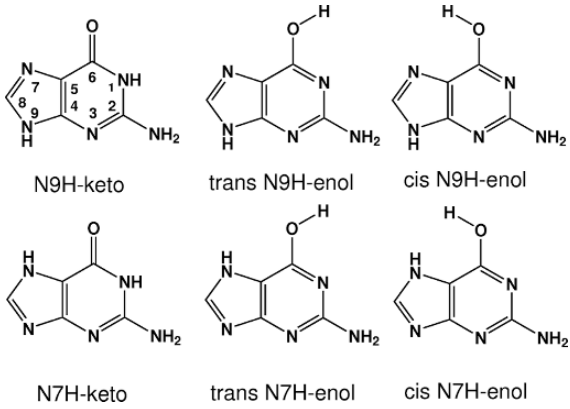

Figure 10-10. Structure and nomenclature of the six most stable G tautomers. The atomic numbering scheme is illustrated for the 9H-keto tautomer

from adiabatic excited state CP-MD simulations demonstrate that anharmonic effects only play a minor role.

Besides the characterisation of the individual G tautomers, CP-MD simulations of the 9H-enol tautomer in the gas phase at various temperatures have been carried out to investigate tautomerisation mechanisms [46]. Spontaneous tautomerisation involving proton transfer is not observable in the time window of a few picoseconds permitted by AIMD even at increased temperature as high as 1000 K. However, frequent *cis–trans* isomerisation events are seen to take place suggesting that the two enol isomers are indistinguishable experimentally.

In a subsequent study, Langer et al. [47] followed the strategy to start with the least stable tautomer, *cis*-7H-enol G, in the hope that its tautomerisation would be more easily accessible to AIMD. However, although *cis*-7H-enol G was calculated to be 63 kJ/mol higher in energy in the S_1 state than the most stable form, 7H-keto G, [43] no tautomerisation could be observed at 300 K on the picosecond time scale.

In order to overcome the reaction barrier within current restrictions of computer time, the hydrogen coordination number of the hydroxylic oxygen was forced to decrease from unity to zero by applying a suitable constraint [47, 88, 89]. By thermodynamic integration it is possible to determine the free energy barrier height for this process [19].

The top panels of Figure 10-11 illustrate that an *isolated* 7H-enol G molecule undergoes a $\pi\pi^*$ (a) to $\pi\sigma^*$ (b) transition when adiabatically evolving in its S_1 state upon enforced elongation of the hydroxylic OH bond ultimately leading to hydrogen detachment (c). It should be mentioned that during the series of constrained excited state AIMD simulations frequent *cis–trans* isomerisations were observed. Surprisingly, however, the hydrogen atom was not seen to re-attach to G to form the 7H-keto species.

Along this OH dissociation coordinate, we also find a conical intersection between the $\pi\sigma^*$ state, S_1, and the ground state, S_0, which could act as an efficient route for internal conversion. Such a scenario has been advocated by Domcke and Sobolewski [23, 84, 86] to be responsible for the photostability of nucleobases. However, in the present case, the free energy activation barrier for OH dissociation was computed to be 52 kJ/mol [47]. Hence this de-excitation pathway is unlikely to explain the ultrafast nonradiative decay observed experimentally [5, 11, 37]. Shukla and Leszczynski [80] find an activation barrier of 154 kJ/mol for the keto–enol tautomerisation of 7H G. However, this result is for tautomerisation in the $\pi\pi^*$ state, whereas the ROKS study involves two different excited states [47].

10.3.3.1.2. Microsolvation In order to systematically study the effects of solvation on the tautomerisation of G, the hydrogen bonded aggregate of 7H-enol G and a single H_2O molecule was investigated before moving to the fully solvated system (see below). Addition of a single water molecule can significantly reduce the activation barrier for proton transfer [4, 49].

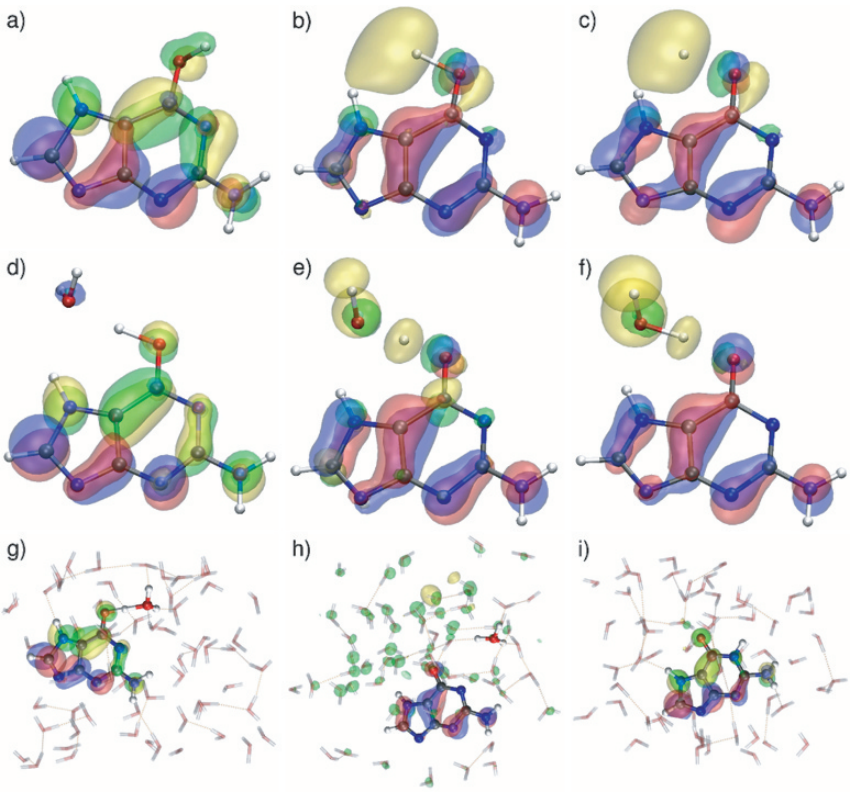

Figure 10-11. Representative trajectory snapshots showing the nuclear skeleton and the two canonical SOMOs (π^*/σ^*: *light grey*, π: *dark grey*) at different stages of OH bond dissociation. *Top panel*: isolated G at an OH distance of 1.11 Å (a), 1.36 Å (b), and 1.62 Å (c). *Middle panel*: G•H_2O at an OH distance of 1.26 Å (d), 1.44 Å (e), and 1.62 Å (f). *Bottom panel*: G(aq) at an OH distance of 1.21 Å (g), 1.59 Å (h), and 1.59 Å (i); note that the identity of the proton that recombines with N to form 7H–keto guanine in (i) is different from the one that was detached from the 7H–enol tautomer in (g) and that a H_3O^+ charge defect migrated through water between (h) and (i)

As for naked G, the enolic OH bond in G•H_2O was also forced to break using constrained AIMD simulations in the S_1 excited state [47]. Snapshots of the resulting reaction pathway are depicted in the middle panels of Figure 10-11. The S_1 wavefunction changes character from $\pi\pi^*$ (d) to $\pi\sigma^*$ at an OH distance of around 1.3 Å (e) accompanied by the formation of a G and H_3O radical pair (f) without, however, featuring a S_0/S_1 conical intersection along this particular dissociation coordinate. At a later stage after numerous *cis–trans* isomerisations the H atom recombines with G to form 7H-keto G. It is worth emphasizing that both the ROKS DFT and previous CASSCF calculations [24, 83, 86] favour hydrogen transfer over proton transfer, i.e. the formation of a radical pair over an ion pair, for a small number of solvent molecules. Sobolewski and Domcke [83], Sobolewski et al. [86]

have shown, however, that the H_3O radical decomposes into a hydronium cation and a solvated electron as the cluster size increases.

The activation barrier for hydrogen abstraction determined from the excited state AIMD simulations is 51 kJ/mol, only slightly lower than for naked G [47]. This may be due to the fact that in the microsolvated case the oxygen–oxygen distance across the $G\cdots H_2O$ hydrogen bond was kept fixed at 2.92 Å in order to avoid trivial dissociation of the hydrogen bond. For the 7H $G\bullet H_2O$ complex, Shukla and Leszczynski [80] report an activation barrier of 56 kJ/mol for the keto–enol tautomerisation of 7H G. Although the two values are in good agreement, they should not be compared directly as they describe different chemical processes. Langer et al. [47] describe a transition form a $\pi\pi^*$ to a $\pi\sigma^*$ state, whereas Shukla and Leszczynski [80] remain on the $\pi\pi^*$ surface throughout.

10.3.3.1.3. Aqueous solution Tautomerisation in aqueous solution is expected to be enhanced by the existence of additional solvent-assisted proton transfer pathways. CP-MD calculations of *cis*-7H-enol G (Figure 10-10) embedded in a periodically repeated unit cell with 60 H_2O molecules have been performed both in the ground state and in the S_1 state. On a time scale of roughly 4 ps, no proton transfer occurred. Analysis of the excited state radial distribution functions for solute–solvent hydrogen bonds at various sites of the G molecule reveals that nitrogen $N^{(9)}$ is the most likely candidate for protonation, closely followed by nitrogen $N^{(1)}$ [46]. By far the most acidic site of the G molecule seems to be the OH group followed by the $N^{(7)}H$ group. However, the calculations indicate that *cis*-7H-enol G in aqueous solution is stable at least on a picosecond time scale. The proton donor sites must therefore be only weakly acidic, whereas the proton acceptor sites are only weakly basic.

Since no spontaneous tautomerisation can be observed on the time scale of the AIMD simulation, possible proton transfer mechanisms have been studied by means of geometric constraint dynamics [47]. Motivated by the observations during the unconstrained simulation, the first objective is to break the enol OH bond, which is apparently the most likely scenario. For this purpose, the coordination number of the oxygen atom is incrementally reduced from a value of approximately unity (corresponding to the unconstrained equilibrium) to zero (corresponding to complete deprotonation). A hydronium ion, H_3O^+, and a solvated electron are formed as the coordination constraint breaks the OH bond. This is in contrast to breaking the OH bond of an isolated or a microsolvated G, where the transferred hydrogen remains intact, i.e. no charge separation occurs [47] (see Sections 10.3.3.1.1 and 10.3.3.1.2), similar to the results of Domcke and Sobolewski [24, 83], Sobolewski et al. [86]. Further reduction of the coordination number then leads to the onset of a Grotthus-type diffusion of the proton through the water solvent. Eventually the proton recombines with the G solute molecule to form the 7H-keto tautomer. From the constrained AIMD simulations a free energy activation barrier of 27 kJ/mol has been determined for OH dissociation [47]. Thus the barrier in solution is approximately half as high as in the gas phase and for the microsolvated $G\bullet H_2O$.

For the unconstrained equilibrium system the S_1 excitation has $\pi\pi^*$ character both SOMOs being localized on the G molecule (see Figure 10-11g). As the OH bond breaks the S_1 excitation becomes $\pi\sigma^*$, the $\sigma^\star$ orbital being delocalized on various solvent water molecules (Figure 10-11h). Upon recombination and formation of the 7H-keto tautomer the S_1 excitation reassumes $\pi\pi^*$ character (Figure 10-11i). Such a mechanism has also been proposed for excited state solute-solvent proton or hydrogen transfer [24, 91]. As in the microsolvated case, no conical intersection between the $\pi\sigma^*$ excited state and the ground state has been found in aqueous solution. Hence there is no efficient pathway for nonradiative decay via hydrogen detachment. Moreover, any involvement of proton or hydrogen transfer in the ultrafast internal conversion mechanism can be ruled out, since the activation barrier is too high. This has been confirmed experimentally for adenine by measuring the same lifetime in H_2O and D_2O, respectively [12].

The AIMD simulation results do not provide any evidence as to whether the 7H-keto tautomer is the energetically preferred form in aqueous solution. In order to determine the relative stabilities of 7H-keto and 9H-keto one would have to apply the constraint to the $N^{(7)}H$ bond and calculate the free energy difference between the two minima.

10.3.3.2. Tautomer-specific photophysical properties

10.3.3.2.1. 9H-keto G In this section we summarize the photophysical properties of the canonical, biologically relevant 9H-keto G tautomer. In contrast to the lower energy 7H-keto form, the excited state dynamics of 9H-keto G is determined by three minima on the S_1 PES characterized by out-of-plane distortions (see Figure 10-12). In configuration space, structure (a) is closest to the optimized ground state global minimum structure, the root mean square distance (RMSD) being 0.07 Å, followed by structure (b) (RMSD=0.11 Å) and the global S_1 minimum (c) (RMSD=0.24 Å). The global minimum (c) characterized by a heavily out-of-plane distorted amino group was first discovered in excited state AIMD simulations of the methylated form of 9H-keto G, i.e. 9Me-keto G [44]. Recently, TDDFT calculations by Marian have confirmed the existence of such a global minimum geometry [53]. Table 10-1 summarizes the energetic and structural data associated with the three S_1 minima. Local minimum (b) whose six-membered ring exhibits a large out-of-plane distortion (Figure 10-12) is only 0.03 eV higher in energy than the global minimum (c).

The mechanism of nonradiative decay has been studied by Langer and Doltsinis [41, 42] using the nonadiabatic AIMD method introduced in Section 1.2. A total

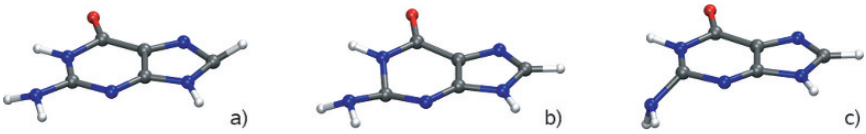

Figure 10-12. Excited state local (a and b) and global (c) minimum structures of 9H-keto G

of 16 surface hopping trajectories, each 1 ps long, were calculated starting from randomly selected points of a ground state trajectory at 300 K. A mono-exponential fit to the time-dependent S_1 ensemble population yields an excited state lifetime of 0.8 ps. The average transition probability and its standard deviation lead to the interval [0.5…0.8…2.2] ps. This agrees nicely with the experimental result of 0.8 ps by Kang et al. [37, 38]. Haupl et al. [33] report lifetimes on the picosecond timescale, while Kohler and co-workers have determined the lifetimes of nucleosides to lie in the subpicosecond range [36]. More recently, Canuel et al. [5] measured a bi-exponential decay with the time constants 148 fs and 360 fs. Chin et al. [11], on the other hand, report fluorescence decay times for various guanine tautomers in the nanosecond regime.

Out-of-plane deformations have been found to considerably enhance the nonadiabatic transition probability, similar to the case of 9Me-keto G [45]. After photoexcitation, the molecules first traverse the largely planar local minimum (a) (Figure 10-12). During this period the transition probability is typically small; it then increases substantially upon entering the local minimum (b) when the six-membered ring becomes strongly nonplanar. This may be explained by the existence of a conical intersection at out-of-plane distorted geometry. Figure 10-13 shows a cut through the S_0 and S_1 potential energy surfaces along the $N^{(2)}C^{(2)}C^{(4)}C^{(5)}$ dihedral angle. A conical intersection can be seen at 97° only 1.0 eV above the Franck-Condon point. Note that the intersection point may be lowered in energy if the structure were allowed to relax in the S_1 state at fixed dihedral angles. Here the remaining degrees of freedom were kept fixed at their S_0 global minimum values. Marian [53] recently located a conical intersection between the $\pi\pi^*$ state and the ground state at a very similar geometry with a $N^{(2)}C^{(2)}C^{(4)}C^{(5)}$ dihedral angle of 94° using TDDFT.

In contrast to all other tautomers investigated, photoexcitation initially takes 9H-keto G to a *local* S_1 minimum. Since the latter is thermally unstable, the system then decays to the global minimum, which is geometrically far from the S_0 structure

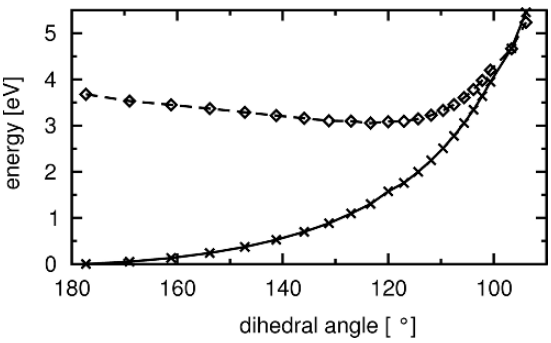

Figure 10-13. Cut through the S_0 (×, *solid line*) and S_1 (◇, *dashed line*) potential energy surfaces of 9H-keto G along the $N^{(2)}C^{(2)}C^{(4)}C^{(5)}$ dihedral angle

giving rise to very poor vertical excitation efficiency. Therefore optical absorption in this spectral region is expected to be comparatively weak. This is corroborated by the fact that only the 7H-keto tautomer has been observed experimentally [61, 62].

10.3.3.2.2. 7H-keto G Although 7H-keto G is not the canonical tautomer, it has the lowest energy both in the ground and in the excited state [43]. Its excited state properties are distinctly different from the 9H-keto tautomer. The S_1 global minimum is largely planar and closely resembles the S_0 structure, the RMSD value being 0.06 Å (see Table 10-1 [41, 42]). The largest changes with respect to the ground state geometry are the elongations of the $C^{(4)}C^{(5)}$ and $N^{(7)}C^{(8)}$ bonds by about 0.1 Å. It has been verified that all three S_1 minima analogous to the 9H-keto structures shown in Figure 10-12 do exist, but only the global minimum (a) has been found relevant to the excited state dynamics (see below). The larger vertical de-excitation energy, $\varepsilon^{\text{fluor}}$, in the case of 7H-keto G compared to 9H-keto G already hints at a slower nonradiative decay.

An ensemble of 16 nonadiabatic surface hopping trajectories have been calculated sampling different initial conditions from a 300 K ground state simulation. A mono-exponential fit to the S_1 population gives a lifetime of 1.0 ps. Estimating the lifetime using the relation (10-13) yields the interval [0.9…1.6 …6.0] ps, which indicates that the result from the exponential fit probably underestimates the lifetime [41, 42]. The 7H-keto tautomer is thus considerably longer lived than the 9H-keto form.

The main driving modes responsible for nonradiative decay have been found to be out-of-plane vibrational motions. In particular the $O^{(6)}C^{(6)}C^{(5)}C^{(4)}$ dihedral describing the out-of-plane motion of the keto oxygen atom and the dihedrals $H^{(7)}N^{(7)}C^{(8)}N^{(9)}$ and $H^{(8)}C^{(8)}N^{(9)}C^{(4)}$ expressing the out-of-plane distortion of the five-membered ring exhibit a good correlation with the surface hopping transition parameter P_{10}.

10.3.3.2.3. 9Me-keto G Replacing a hydrogen atom in G by a methyl group has been shown experimentally to have only minor effects on the S_1 optical absorption spectra for most tautomers. For a number of years it was thought that methylation of 9H-keto G drastically changes its photophysical properties since the 9Me-keto tautomer had proven impossible to detect while the 9H-keto tautomer had been (wrongly) identified in supersonic jets [61, 67, 77]. ROKS calculations by Langer and Doltsinis [44] suggest that the excited state global minimum structure of 9Me-keto G is heavily distorted compared to the ground state (analogous to Figure 10-12c) and therefore the optical absorption signal should be smeared out and/or the probability for absorption should be low. Langer and Doltsinis [44] concluded that there is a marked difference between the methylated and unmethylated species in this respect, but their judgement was based on the assumption that structure (b) of Figure 10-12 is the global S_1 minumum of 9H-keto G. Excited state geometry optimization by Černý et al. [99] using TDDFT also produced an out-of-plane distorted structure; however the deformations mainly concerned the $N^{(9)}H^{(9)}$ imino group.

In a series of AIMD runs at fixed temperatures between 10 and 50 K, it has been shown that initially after photoexcitation 9Me-keto G travels through a local

S_1 minimum (cf. Figure 10-12a), where it can be trapped at temperatures lower than 50 K. In a realistic scenario, however, the system gathers enough momentum during the initial ballistic phase after vertical excitation to be able to leave this local minimum and thus it eventually ends up in the geometrically distant global S_1 minimum (cf. Figure 10-12c) via the local minimum (b) (cf. Figure 10-12). As a consequence, the overlap between the S_0 and S_1 nuclear wavefunctions and therefore the absorption probability are expected to be small.

Langer and Doltsinis [45] have calculated nonadiabatic surface hopping trajectories for 10 different initial configurations sampled from a ground state AIMD runs at 100 K. They later extended their study to a total of 16 trajectories [41, 42]. From a mono-exponential fit to the S_1 population a lifetime of 1.3 ps is obtained (see Table 10-1; the average transition probability and its standard deviation leads to the interval [0.6…1.1…3.5] ps. Thus methylation appears to result in a slightly longer excited state lifetime.

The nonadiabatic hopping probability has been analysed as a function of time and correlated with individual vibrational modes (see Figure 10-14). After approximately 40 fs, a steep rise in the hopping probability of 9Me-keto G is observed marking the transition from the first, planar local minimum structure (a) to the second local minimum (b) from where the system relaxes into the global S_1 minimum (c). The strong enhancement of nonadiabatic coupling for 9Me-keto G

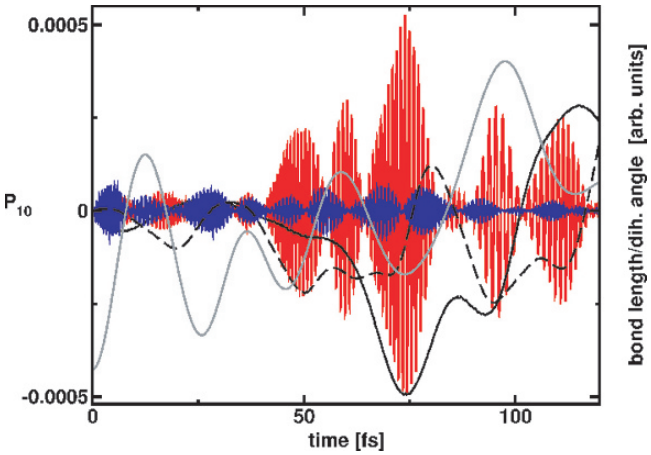

Figure 10-14. Time evolution of the nonadiabatic surface hopping parameter, P_{10} (Eq. 10-10), for a transition from the S_1 excited state to the S_0 ground state for representative 7Me-keto (fast oscillating, small amplitude dark *grey curve*) and 9Me-keto (fast oscillating, large amplitude light *grey curve*) G trajectories. The steep increase of P_{10} at $t \approx 40$ fs in the case of 9Me-keto coincides with the transition from a quasi-planar to an out-of-plane distorted structure. At $t \approx 40$ fs the amino group starts rotating such that one of its NH bonds is in plane. A measure of this motion are the temporal changes in the dihedral angle $H^{(b)}N^{(2')}C^{(2)}N^{(1)}$ (- -). Shortly after, out-of-plane distortion of the six-membered ring sets in as indicated by the $C^{(2)}N^{(1)}C^{(5)}C^{(4)}$ dihedral angular velocity (——). The fine structure of P_{10} is caused by $C^{(2)}N^{(3)}$ bond length oscillations (——)

in this phase is due to the onset of massive out-of-plane structural distortions. As a preparatory step in order to leave the quasi-planar 9Me-*keto* local S_1 minimum (a), the amino group rotates such that one of its NH bond lies in the skeletal plane. Only then out-of-plane distortions of the six-membered ring set in. The higher frequency modulation of the P_{10} curve can be explained by oscillations in the $C^{(2)}N^{(3)}$ bond length (see Figure 10-14).

10.3.3.2.4. 7Me-keto G Langer and Doltsinis have also investigated the methylated form of the 7H-keto tautomer, 7Me-keto G. Its global S_1 excited state potential energy minimum closely resembles that of the unmethylated 7H-keto G, which is reflected in the data presented in Table 10-1 [44, 45].

Nonadiabatic ab initio surface hopping simulations were carried out for 11 different starting points taken from a ground state run at 100 K. The excited state nonradiative lifetime has been determined to be 1.7 ps from an exponential fit to the S_1 population decay (Eq. (10-11)) and to lie in the interval [1.7…3.1…13.4] ps using the average transition probability (Eq. (10-13)).

Figure 10-14 demonstrates that typically the nonadiabatic transition parameter (10-10) is smaller compared to the 9Me-keto tautomer. In particular, due to the absence of any large out-of-plane deformations, there is no steep increase at about 40 fs. This explains why 7Me-keto G is somewhat longer lived than 9Me-keto G. Both methylated tautomers exhibit longer excited state nonradiative lifetimes than their unmethylated counterparts.

10.3.3.2.5. 9H-keto G in liquid water A ground state simulation of 9H-keto G embedded in 60 H_2O molecules in a periodic setup at 300 K has been performed from which six configurations have been randomly selected as input for 6 nonadiabatic surface hopping trajectory calculations starting in the S_1 excited state. Comparison with the simulations in the gas phase (see Section 10.3.3.2.1) permits analysis of the effects of the water solvent on the mechanism of radiationless decay.

The nonadiabatic transition probabilities have the same order of magnitude in the gas phase and in solution. Using relation (10-13) a lifetime interval of [1.1…2.0…12.1] ps has been obtained [41, 42], roughly twice as long as for the gas phase. Of course, in order to obtain a meaningful statistically averaged result for solvated G, e.g. for the excited state lifetime, a larger number of trajectories need to be calculated. Experimentally, Percourt et al. [73] have measured the lifetime of the G nucleoside to be 0.46 ps; Peon and Zewail obtained 0.86 ps for the nucleotide [72]. It is conceivable, however, that a tautomeric species other than the 9H-keto form predominates in aqueous solution [32]. A look at Figure 10-15 reveals significant qualitative differences between the excited state dynamics in the gas phase and in solution. At any moment in time during the simulations the instantaneous structure is assigned to one of the three S_1 minima shown in Figure 10-12 according to whose RSMD is smallest. The upper panel of Figure 10-15 shows how in the gas phase the number of trajectories populating the initial local minimum (Figure 10-12a) rapidly decreases in the first approximately 100 fs, while the more

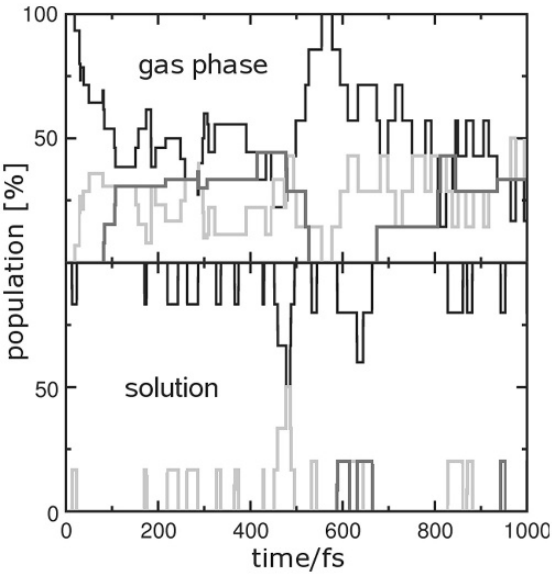

Figure 10-15. Percentage of trajectories populating the three different excited state minima (see Figure 10-12) as a function of time in the gas phase and in solution
The *black line* shows the population of local minimum (a), the light *grey line* the population of local minimum (b), and the dark *grey line* that of the global minimum (c)

stable minima (b) and (c) (Figure 10-12) are successively populated. Note that after about 500 fs population (a) seems to have increased again, but this is merely due to the fact that a large portion of those trajectories occupying minima (b) or (c) have already decayed to the ground state.

The analogous procedure applied to the ensemble of solution phase trajectories gives a very different picture (see lower panel of Figure 10-15). It can be seen that the vast majority of trajectories get stuck in minimum (a) (Figure 10-12) and the out-of-plane distorted structures (b) and (c) hardly occur. Whether this is due to a destabilization of the latter two minima by the solvent or to an increase of the barrier height inbetween them and minimum (a) has not been investigated. Shukla and Leszczynski [81] show for G•$(H_2O)_n$ ($n = 0, \ldots, 7$) clusters that for $n > 5$ the structure of G becomes increasingly planar, which corroborated the AIMD findings in aqueous solution.

10.3.4. Guanine-Cytosine Base Pair

10.3.4.1. Nonradiative decay in the gas phase

10.3.4.1.1. Excited state potential and lifetime Markwick et al. [56] have studied possible tautomerisation events involving (multiple) proton transfer using the unbiased, collective *dynamic distance constraint* method. While in the ground

state a double proton transfer process was observed, in the S_1 state a single coupled proton–electron transfer reaction transferring the central $H^{(1')}$ atom from G to C (see Figure 10-16) was predicted [56]. Figure 10-17 shows the S_0 and S_1 energies along the excited state minimum energy path for this process. The charge transfer (CT) product state is lower in energy than the locally excited state by 0.4 eV, the two minima being separated by a very shallow activation barrier (the free energy value is 0.14 eV). At the CT geometry, the $S_0 - S_1$ energy gap is seen to be small (see also Table 10-1), suggesting that there might be an efficient path for nonradiative relaxation in the vicinity. Figure 10-17 further illustrates that at finite temperature the energy gap at the CT minimum decreases demonstrating the importance of a dynamic treatment.

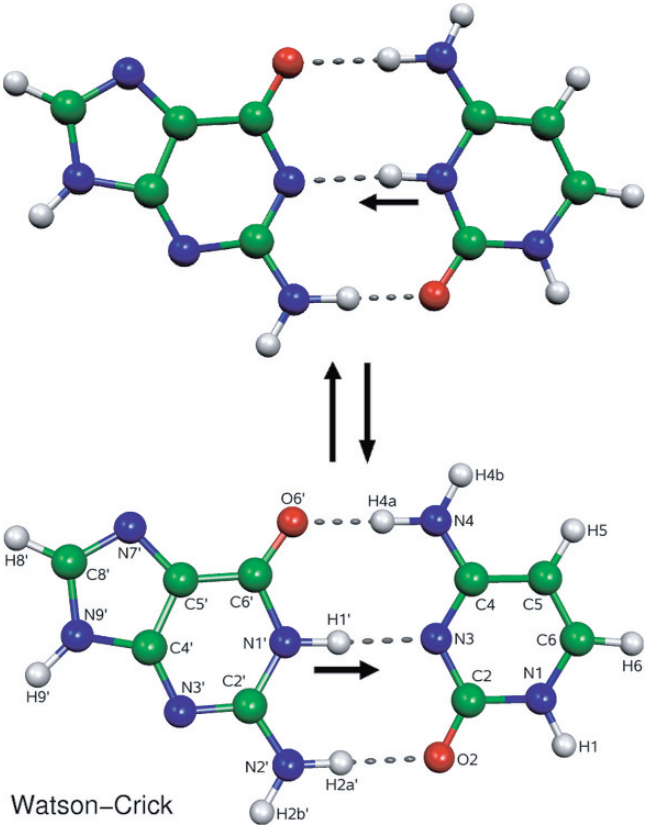

Figure 10-16. Reactant (Watson-Crick) and product GC structures of the excited state proton transfer reaction. The atom numbering scheme is illustrated for the initial Watson-Crick configuration

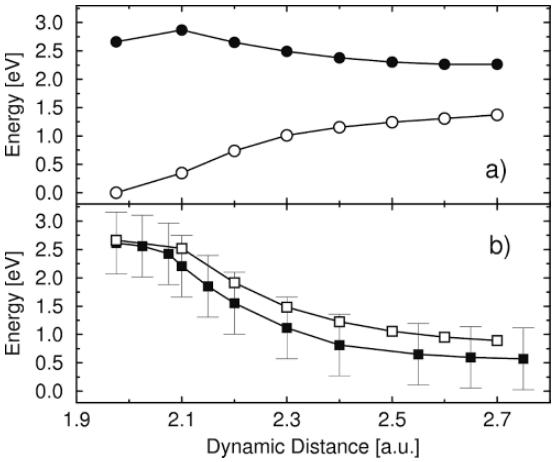

Figure 10-17. a) Ground (*open circles*) and excited (*closed circles*) state energy profiles along the S_1 MEP of GC. (b) Average $S_0 - S_1$ energy difference as a function of the dynamic distance at 300 K (*closed squares*) compared to the MEP values (*open squares*)

For various snapshots along the reaction coordinate the singly occupied molecular orbitals (SOMOs) which characterize the electronic excitation, have been analyzed (see Figure 10-18). At the initial Watson–Crick (WC) geometry the electronic excitation is seen to be mostly localized on G. However, a transition of electron density from G to C is clearly observed when the transition state is approached. This is in agreement with other ab initio calculations [85, 87]. It is interesting to note that the transfer of the electron occurs prior to that of the proton. This can be deduced from the highest energy SOMO at the transition state (Figure 10-18); it is seen to be fully localized on C.

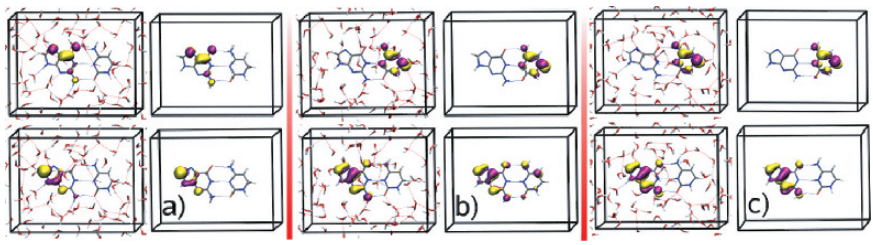

Figure 10-18. Singly occupied molecular orbitals (SOMOs) of the S_1 excited state for snapshots from constraint simulations of GC in aqueous solution at the Watson-Crick (a), transition state (b), and charge transfer (c) geometries. For each snapshot the SOMOs in aqueous solution are compared to a gas phase calculation using the same G-C geometry

From a theoretical point of view, a balanced description of the initially excited local $\pi\pi^*$ on one side of the barrier and the $\pi\pi^*$ CT state on the other side is a big challenge, even for the CASSCF and CASPT2 methods [29, 85]. The potential curve including the barrier height predicted by the ROKS method [56] is remarkably close to the CC2 result of Ref. [87].

Markwick and Doltsinis [55] have calculated 60 nonadiabatic surface hopping trajectories starting from different intial coordinates and velocites obtained from snapshots of a ground state CP-MD simulation at 300 K. Figure 10-19 shows the excited state population as a function of time after vertical photoexcitation for the swarm of 60 trajectories. From a bi-exponential fit (10-12) to the data points the two characteristic time constants for nonradiative decay, $\tau_1 = 31 \pm 4$ fs and $\tau_2 = 293 \pm 49$ fs, have been derived. The uncertainty in the decay constants given here merely relates to the fitting error and does not account for any systematic errors associated with the simulation method. Interestingly, a mono-exponential fit yields a decay time of $\tau = 89 \pm 8$ fs. As can be clearly seen from Figure 10-19, the mono-exponential fit describes the simulation data rather poorly, whereas the bi-exponential fit reproduces the data points very well.

The theoretical S_1 nonradiative lifetimes by Markwick and Doltsinis [55] are in agreement with recent experimental observations [2, 79] which suggest that the canonical base pairs are extremely short-lived, the GC lifetime being of the order of 100 fs. This is also in accord with the scenario sketched by ab initio

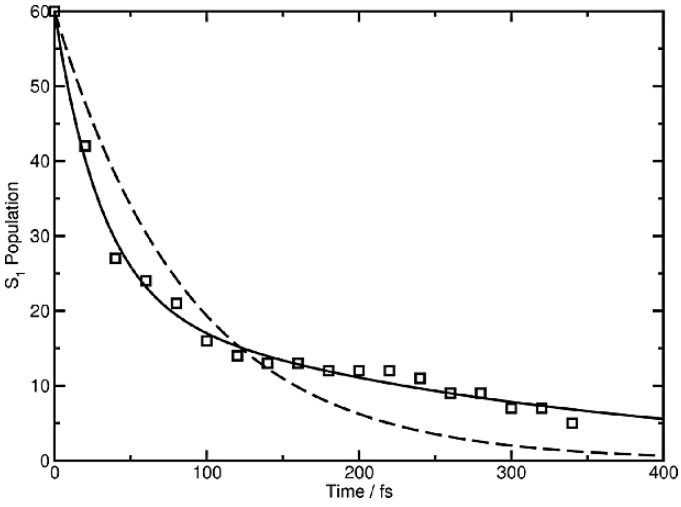

Figure 10-19. Excited state population (*squares*) of the GC base pair in the gas phase as a function of time after vertical photoexcitation. Nonradiative lifetimes of $\tau_1 = 31 \pm 4$ fs and $\tau_2 = 293 \pm 49$ fs have been determined from a bi-exponential fit (*solid line*); a mono-exponential fit (*dashed line*) gives a lifetime of 89 ± 8 fs

calculations [29, 56, 85, 87] indicating that there is a nearly barrierless PT reaction path in the S_1 state leading to a $S_0 - S_1$ conical intersection. We note that the recent CASSCF-based surface hopping calculations by Groenhof et al. [29] yield a lifetime of 90 fs, very close to the mono-exponential fit of Figure 10-19. A detailed analysis of the nonradiative decay mechanism from nonadiabatic AIMD simulations [55] will be presented below.

10.3.4.1.2. Time-evolution of the $S_0 - S_1$ energy gap The energy gap, ΔE, between the S_0 ground state and the S_1 excited state is usually considered to be an important parameter controlling the nonadiabatic coupling strength. The time-evolution of ΔE for a typical surface hopping trajectory is shown in Figure 10-20. After vertical photoexcitation at time $t = 0$, a rapid decrease of the $S_0 - S_1$ energy gap by nearly 3 eV is observed, reaching a first minimum of about 0.5 eV at $t \approx 10$ fs (see Figure 10-20). Thereafter, the energy gap is seen to fluctuate about a small value almost vanishing at $t \approx 88$ fs. Is it possible to attribute these temporal changes of ΔE to certain molecular motions?

Three internal degrees of freedom have been identified which exhibit a direct and strong correlation with the temporal changes of ΔE as the system evolves on the excited state potential surface. These three geometric variables are the $H^{(1')}N^{(3)}$ interatomic distance, R(NH), and the two dihedral angles $C^{(6')}O^{(6')}N^{(4)}C^{(4)}$ and $H^{(4b)}N^{(4)}C^{(4)}C^{(5)}$, referred to from here on as Θ and Φ, respectively. The variation with time in the energy gap and these degrees of freedom are shown in Figure 10-20. The upper panel of Figure 10-20 illustrates the correlation between ΔE and R(NH).

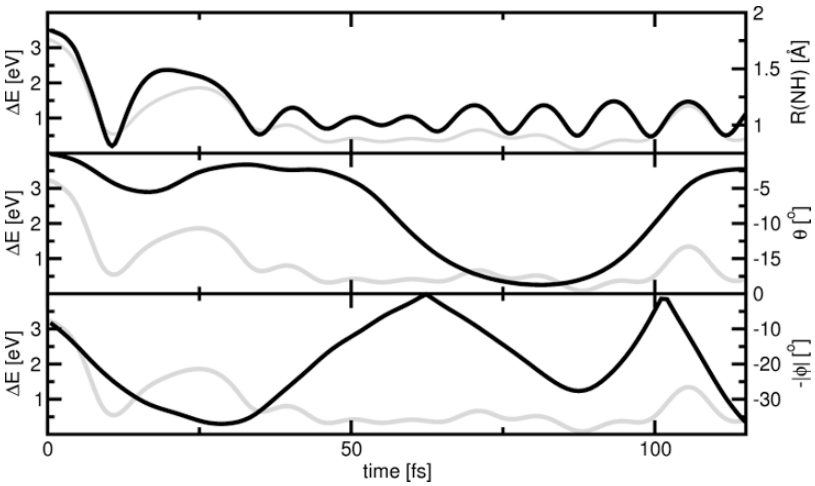

Figure 10-20. Comparison of the energy gap ΔE (*grey lines*) and the $H^{(1')}N^{(3)}$ distance R(NH) (*top panel, black line*), the $C^{(6')}O^{(6')}N^{(4)}C^{(4)}$ dihedral angle (*middle panel, black line*), and the $H^{(4b)}N^{(4)}C^{(4)}C^{(5)}$ dihedral angle (*bottom panel, black line*) for a typical surface hopping trajectory of GC

In particular during the first 35 fs both curves have extremely similar shapes. The rapid decrease of ΔE in the first 10 fs is accompanied by the coupled proton–electron transfer of $H^{(1')}$ across the central hydrogen bond. The distance R(NH) quickly falls from its intial value of 1.84 Å to 0.81 Å at $t = 10$ fs. At 5 fs, the hydrogen atom $H^{(1')}$ is mid-way between G and C. The proton then bounces back away from $N^{(3)}$ such that R(NH) increases again towards 1.5 Å and then vibrates back to about 0.95 Å. This is co-incident with the increase and decrease in the energy gap between 10 fs and 30 fs. The kinetic energy gained by the relaxation into the CT state is initially concentrated in the $H^{(1')}N^{(3)}$ vibration, but is subsequently redistributed to other degrees of freedom.

The middle panel of Figure 10-20 shows a comparison of the time-evolution of the $C^{(6')}O^{(6')}N^{(4)}C^{(4)}$ dihedral angle, Θ, and ΔE. After about 50 fs, Θ starts to deviate significantly from zero bringing the system away from planarity. We notice that at the moment when ΔE is smallest ($t \approx 88$ fs) the molecular structure is highly non-planar with $\Theta \approx -18°$. Furthermore, the peak in ΔE at about 106 fs coincides with a small absolute value of Θ, i.e. near-planarity of the molecule.

The third important parameter influencing the energy gap is the $H^{(4b)}N^{(4)}C^{(4)}C^{(5)}$ dihedral angle, Φ, a measure for the out-of-plane distortion of the amino group on C. The negative absolute value of Φ is plotted in the bottom panel of Figure 10-20. It appears that a pronounced out-of-plane distortion is a prerequisite to reach the $S_0 - S_1$ conical intersection. For instance, at $t \approx 88$ fs, when ΔE is minimum, both Φ and Θ are pronouncedly non-zero and close to their respective maximum amplitudes. When ΔE peaks at 106 fs both dihedrals are significantly closer to zero. Markwick and Doltsinis [55] conclude that the $H^{(1')}N^{(3)}$ distance has the strongest influence on ΔE; however, the conical intersection becomes accessible only through constructive interference of the $H^{(1')}N^{(3)}$ vibration with out-of-plane motions.

10.3.4.1.3. Time-evolution of the nonadiabatic transition probability Having analyzed the time-dependence of the $S_0 - S_1$ energy gap and the way in which it is affected by specific molecular vibrations, how is the behaviour of ΔE reflected in the nonadiabatic transition probability? The time-evolution of the surface hopping transition parameter P_{10} (Eq. 10-10) is shown in Figure 10-21. First of all, it is important to note that the amplitudes of the P_{10} signal are *not* directly correlated to the ΔE curve of Figure 10-20. However, as demonstrated in the first panel of Figure 10-21, the time-derivative of ΔE almost perfectly reproduces the envelope of P_{10}. Once the correlation of P_{10} and $d(\Delta E)/dt$ has been established, it follows that the time-derivatives of the three internal degrees of freedom discussed in the previous section must also be correlated to P_{10}. This is shown in the lower three panels of Figure 10-21.

Initially, a very large amplitude of P_{10} is observed between 5 fs and 10 fs, followed by a secondary maximum at about 13 to 16 fs and a third local maximum

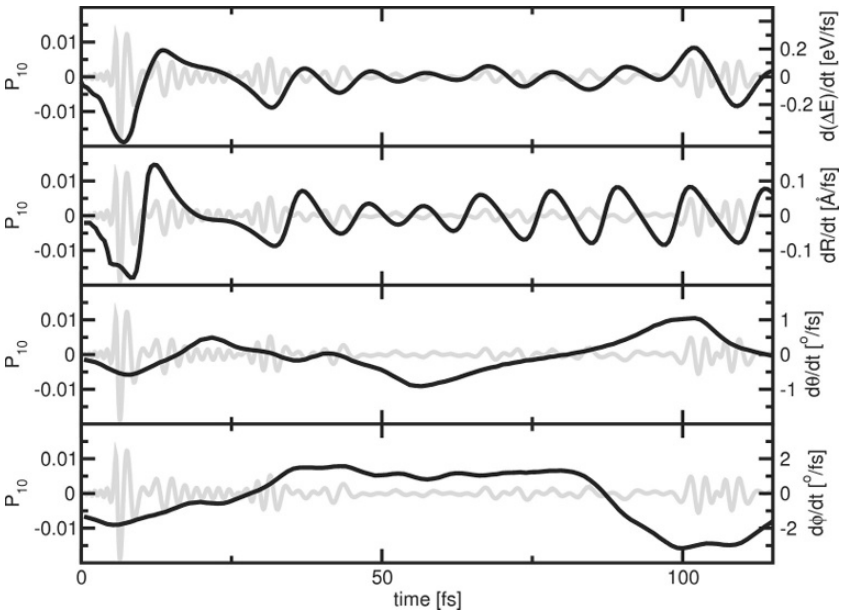

Figure 10-21. Comparison of the nonadiabatic transition parameter, P_{10} (see Eq. 10-10, *grey lines*), and the time-derivatives (*black lines*) of the energy gap ΔE(*first panel*), the $H^{(1')}N^{(3)}$ distance (*second panel*), the $C^{(6')}O^{(6')}N^{(4)}C^{(4)}$ dihedral angle (*third panel*), and the $H^{(4b)}N^{(4)}C^{(4)}C^{(5)}$ dihedral angle (*fourth panel*) for a typical surface hopping trajectory of GC

at about 30 fs. These maxima all exactly coincide with the extrema of the time-derivative of the $H^{(1')}N^{(3)}$ interatomic distance (see Figure 10-21, second panel). Between 45 fs and 65 fs, the absolute magnitude of P_{10} is rather small and the time-derivative of R(NH) is small in this region. From 65 to 120 fs, the temporal derivative of R(NH) becomes somewhat larger, and P_{10} is slightly larger in this region compared to the region 45–65 fs.

Once again, later on in the trajectory other features affect the magnitude of P_{10}: The most significant feature in the profile of P_{10} on the right half of Figure 10-21 is between 100 and 110 fs, when the magnitude of P_{10} exhibits a local maximum. This obviously is not due to $dR(\mathrm{NH})/dt$, but rather to the large amplitudes of $d\Theta/dt$ (Figure 10-21, third panel) and $d\Phi/dt$ (Figure 10-21, fourth panel), the latter reaching a value of over 3 degrees/fs. It is also noticeable that the magnitude of P_{10} is dominated more by $d\Phi/dt$ than $d\Theta/dt$. This may simply be because the time-derivative of Φ is larger than that of Θ. Despite this, one can also discern that P_{10} between 100 and 105 fs is slightly larger than between 105 and 110 fs. The region 100–105 fs is when both $d\Theta/dt$ is greater than 1.0 degrees/fs and $d\Phi/dt$ is greater than 3.0 degrees/fs.

On the grounds of the analysis presented Markwick and Doltsinis [55] explain the existence of a bi-exponential excited state decay function (see Figure 10-19). The

fast process, with an exponential coefficient of 31 fs is concerned with the initial fast coupled proton–electron transfer event and the resulting relaxation into the S_1 CT state. As we have seen in Section 10.3.4.1.3, this process involves massive variations in both the energy gap ΔE and the $H^{(1')}N^{(3)}$ distance. It is clear that the coupled proton–electron transfer also induces large changes in the wavefunctions of ground and excited state, such that the nonadiabatic coupling elements (10-8) become large. As soon as the system has settled into the CT state and redistributed a good part of the excess kinetic energy, the temporal changes in the wavefunctions become much smaller and a second decay component becomes relevant.

The secondary, slower process with an exponential coefficient of 293 fs is concerned more with nonadiabatic transitions out of the CT state, where out-of-plane structural fluctuations play a more significant role. Indeed, this time-scale seems appropriate, as the time for a phase cycle of these out-of-plane motions (Θ and Φ) is of the order of 100 to 200 fs, and P_{10} is observed to have the largest magnitude when both time-derivatives ($d\Theta/dt$ and $d\Phi/dt$) are large concurrently.

10.3.4.2. Nonradiative decay in aqueous solution

In order to study the influence of an aqueous environment on radiationless decay in GC, 10 nonadiabatic surface hopping simulations for the GC base pair in explicit water solvent have been performed [55]. The periodic simulation unit cell containing GC and 57 H_2O molecules can be seen in Figure 10-18, which further illustrates that the electronic excitation has $\pi\pi^*$ character and is well-localized on GC without spilling out into the solvent. Thus, as far as the qualitative picture is concerned, the GC photocycle in liquid water is very similar to that in the gas phase. One of the effects of the solvent environment is to increase the vertical excitation gap by about 0.2 eV on average compared to the gas-phase results, such that the initial value of ΔE in the solvent simulations is on average 3.6 eV, compared to an average gas-phase simulation value of 3.4 eV. In the CT state, on the other hand, the average value for the energy gap in solution is smaller than in the gas phase by about 0.2 eV (see Table 10-1). These findings mean that there is an overall increase in energy difference between vertical excitation and CT state in solution, which should slightly enhance nonradiative decay and thus photostability.

On the basis of the ensemble of 10 surface hopping trajectories an excited state lifetime in aqueous solution of $\tau = 115 \pm 9$ fs has been estimated assuming mono-exponential decay [55]. Fitting a bi-exponential function yields a fast component of $\tau_1 = 29 \pm 9$ fs and a slow component of $\tau_2 = 268 \pm 62$ fs [55]. These results are very similar to the gas phase values. However, the latter should be considered to be much more accurate due to the much larger number of trajectories.

Changes in the energy gap, ΔE, and the nonadiabatic transition probability, P_{10}, in the aqueous solution simulations are dominated in the initial stages by the coupled proton–electron transfer event and the subsequent relaxation of the system into the excited CT state. Similar to the gas phase, variations in ΔE and P_{10} at longer time-scales were found to depend strongly on the out-of-plane motions of the system (for instance the dihedral angles Θ and Φ). However, the presence of

solvent is observed to dampen these out-of-plane motions, such that the variation of ΔE in the charge transfer state is slightly smaller than that in the gas-phase simulations and hence the average magnitude of P_{10} is also slightly smaller for those trajectories that remain in the S_1 state for longer times.

In summary, there exists a very efficient mechanism in the canonical, Watson-Crick form of the GC DNA base pair by which UV radiation can be absorbed without inducing structural damage. Following photoexcitation, an ultrafast coupled proton–electron transfer along the central hydrogen bond takes place leading to a conical intersection region where the system rapidly returns to the ground state in well under a picosecond. Back in the electronic ground state a reverse proton–electron transfer takes place reforming the original Watson-Crick structure. The ultrafast photocycle described here may indeed be responsible for the photostability of DNA.

10.4. CONCLUSIONS

We have presented nonadiabatic ab initio molecular dynamics simulations of the photophysical properties of a variety of nucleobases and base pairs. In addition to the canonical tautomers a number of rare tautomers have been investigated. Moreover, effects of substitution and solvation have been studied in detail. The simulations of nonradiative decay in aqueous solution, in particular, demonstrate the strength of the na-AIMD technique employed here as it permits the treatment of solute and solvent on an equal footing. Condensed phase calculations can be directly compared with those in the gas phase because the same computational setup can be used.

The excited state lifetimes determined from the na-AIMD simulations are generally in good agreement with experimental data. In addition, the na-AIMD simulations provide detailed insights into the dynamical mechanism of radiationless decay. The time evolution of the nonadiabatic transition probability could be correlated with certain vibrational motions. In this way, the simulations yield the driving modes of internal conversion.

In an oversimplified picture, nonradiative decay in U and C is controlled by a torsional motion about the $C^{(5)}C^{(6)}$ double bond, while in the canonical G tautomer out-of-plane deformations of the six-membered ring are chiefly responsible for internal conversion. In the case of G, the canonical, biologically relevant, 9H-keto form indeed exhibits photophysical properties which are distinctly different from other tautomers. Its excited state lifetime, for example, is the shortest of all tautomers. This is a consequence of its pronounced out-of-plane distortions absent in other tautomers.

Methylation has been found to prolong the lifetime of both the 9H-keto and the 7H-keto form of G. In the case of C, methylation stabilizes a dark $n\pi^*$ state which decays rapidly.

In aqueous solution, nonradiative decay of 9H-keto G is slowed down considerably due to the fact that the crucial out-of-plane motions are damped and the

excited state structure of G remains largely planar. For U, on the other hand, the decay mechanisms in solution and in the gas phase are qualitatively the same.

In the canonical GC base pair, radiationless decay is governed by a rather different scenario. Photoexcitation first induces a coupled proton–electron transfer from G to C. The resulting charge transfer state is close to a conical intersection providing an efficient route for internal conversion. Back in the ground state the original Watson-Crick structure is restored rapidly. This ultrafast photocycle may indeed protect nucleic acids from suffering radiation induced damage.

10.5. ACKNOWLEDGEMENTS

We are grateful to the German Science Foundation for funding this work. NIC Jülich, RWTH Aachen, and `BOVILAB@RUB` are acknowledged for computer time.

REFERENCES

1. Hutter J et al. (2007) Car–Parrinello Molecular Dynamics: An *Ab Initio* Electronic Structure and Molecular Dynamics Program, see `www.cpmd.org`.
2. Abo-Riziq A, Grace L, Nir E, Kabelac M, Hobza P, de Vries MS (2005) Proc Natl Acad Sci USA 102:20.
3. Becke AD (1988) Phys Rev A 38:3098.
4. Bell RL, Taveras DL, Truong TN, Simons J (1997) Int J Quantum Chem 63:861.
5. Canuel C, Mons M, Piuzzi F, Tardivel B, Dimicoli I, Elhanine M (2005) J Chem Phys 122:074,316.
6. Car R, Parrinello M (1985) Phys Rev Lett 55:2471.
7. Chargaff E (1950) Experientia 6:201.
8. Chargaff E (1970) Experientia 26:810.
9. Chargaff E (1971) Science 172:637.
10. Chen H, Li S (2006) J Phys Chem A 110:12360.
11. Chin W, Mons M, Dimicoli I, Tardivel B, Elhanine M (2002) Eur Phys J D 20:347.
12. Cohen B, Hare PM, Kohler B (2003) J Am Chem Soc 125:13594.
13. Cohen B, Crespo-Hernández CE, Kohler B (2004) Faraday Discuss 127:137.
14. Crespo-Hernández CE, Cohen B, Hare PM, Kohler B (2004) Chem Rev 104:1977.
15. Doltsinis NL (2002) In: Grotendorst J, Marx D, Muramatsu A (eds) Quantum Simulations of Complex Many-Body Systems: From Theory to Algorithms, NIC, FZ Jülich, www.fz-juelich.de/nic-series/volume10/doltsinis.pdf.
16. Doltsinis NL (2004) Mol Phys 102:499.
17. Doltsinis NL (2004) Faraday Discuss 127:231.
18. Doltsinis NL (2006) In: Grotendorst J, Blügel S, Marx D (eds) Computational Nanoscience: Do it Yourself!, NIC, FZ Jülich, www.fz-juelich.de/nic-series/volume31/doltsinis1.pdf.
19. Doltsinis NL (2006) In: Grotendorst J, Blügel S, Marx D (eds) Computational Nanoscience: Do it Yourself!, NIC, FZ Jülich, www.fz-juelich.de/nic-series/volume31/doltsinis2.pdf.
20. Doltsinis NL, Fink K (2005) J Chem Phys 122:087101.
21. Doltsinis NL, Marx D (2002) Phys Rev Lett 88:166402.
22. Doltsinis NL, Marx D (2002) J Theor Comput Chem 1:319–349.
23. Doltsinis NL, Sprik M (2003) Phys Chem Chem Phys 5:2612.

24. Domcke W, Sobolewski AL (2003) Science 302:1693.
25. Domcke W, Yarkony DR, Köppel H (2004) Conical Intersections: Electronic Structure, Dynamics and Spectroscopy, World Scientific, Singapore.
26. Frank I, Hutter J, Marx D, Parrinello M (1998) J Chem Phys 108:4060.
27. Grimm S, Nonnenberg C, Frank I (2003) J Chem Phys 119:11574.
28. Grimm S, Nonnenberg C, Frank I (2003) J Chem Phys 119:11585.
29. Groenhof G, Schäfer LV, Boggio-Pasqua M, Goette M, Grubmüller H, Robb MA (2007) J Am Chem Soc 129:6812.
30. Gustavsson T, Bányász A, Lazzarotto E, Markovitsi D, Scalmani G, Frisch MJ, Barone V, Improta R (2006) J Am Chem Soc 128:607.
31. Ha TK, Keller HJ, Gunde R, Gunthard HH (1999) J Phys Chem A 103:6612.
32. Hanus M, Ryjáček F, Kabeláč M, Kubar T, Bogdan TV, Trygubenko SA, Hobza P (2003) J Am Chem Soc 125:7678.
33. Häupl T, Windolph C, Jochum T, Brede O, Hermann R (1997) Chem Phys Lett 280:520.
34. He Y, Wu C, Kong W (2004) J Phys Chem A 108:943.
35. Hutter M, Clark T (1996) J Am Chem Soc 118:7574.
36. Ismail N, Blancafort L, Olivucci M, Kohler B, Robb MA (2002) J Am Chem Soc 124:6818.
37. Kang H, Lee KT, Jung B, Ko YJ, Kim SK (2002) J Am Chem Soc 124:12958.
38. Kang H, Jung B, Kim SK (2003) J Chem Phys 118:6717.
39. Kim NJ, Jeong G, Kim YS, Sung J, Kim SK (2000) J Chem Phys 113:10051.
40. Kistler KA, Matsika S (2007) J Phys Chem A 111:2650.
41. Langer H 2006 Dissertation, Ruhr-Universität Bochum.
42. Langer H, Doltsinis NL In preparation.
43. Langer H, Doltsinis NL (2003) J Chem Phys 118:5400.
44. Langer H, Doltsinis NL (2003) Phys Chem Chem Phys 5:4516.
45. Langer H, Doltsinis NL (2004) Phys Chem Chem Phys 6:2742.
46. Langer H, Doltsinis NL, Marx D (2004) In: Wolf D, Münster G, Kremer M (eds) NIC Symposium 2004, NIC, FZ Jülich, for downloads see `http://www.fz-juelich.de/nic-series/volume20/doltsinis.pdf`.
47. Langer H, Doltsinis NL, Marx D (2005) Chemphyschem 6:1734.
48. Lee C, Yang W, Parr RC (1988) Phys Rev B 37:785.
49. Liang W, Li H, Hu X, Han S (2004) J Phys Chem A 108:10219.
50. Lorentzon J, Fülscher MP, Roos BO (1995) J Am Chem Soc 117:9265.
51. Lührs DC, Viallon J, Fischer I (2001) Phys Chem Chem Phys 3:1827.
52. Malone RJ, Miller AM, Kohler B (2003) Photochem Photobiol 77:158.
53. Marian CM (2007) J Phys Chem A 111:1545.
54. Marian CM, Schneider F, Kleinschmidt M, Tatchen J (2002) Eur Phys J D 20:357.
55. Markwick PRL, Doltsinis NL (2007) J Chem Phys 126:175102.
56. Markwick PRL, Doltsinis NL, Schlitter J (2007) J Chem Phys 126:045104.
57. Marx D, Hutter J (2000) In: Grotendorst J (ed) Modern Methods and Algorithms of Quantum Chemistry, NIC, Jülich, `www.theochem.rub.de/go/cprev.html`.
58. Matsika S (2004) J Phys Chem A 108:7584.
59. Mennucci B, Toniolo A, Tomasi J (2001) J Phys Chem A 105:7126.
60. Merchán M, Serrano-Andrés L (2003) J Am Chem Soc 125:8108.
61. Mons M, Dimicoli I, Piuzzi F, Tardivel B, Elhanine M (2002) J Phys Chem A 106:5088.
62. Mons M, Piuzzi F, Dimicoli I, Gorb L, Leszczynski J (2006) J Phys Chem A 110:10921.
63. Müller U, Stock G (1997) J Chem Phys 107:6230.
64. Nieber H, Doltsinis NL (2008) Chem Phys In press.

65. Nir E, Grace L, Brauer B, de Vries MS (1999) J Am Chem Soc 121:4896.
66. Nir E, Kleinermanns K, de Vries MS (2000) Nature 408:949.
67. Nir E, Janzen C, Imhof P, Kleinermanns K, de Vries MS (2001) J Chem Phys 115:4604.
68. Nir E, Kleinermanns K, Grace L, de Vries MS (2001) J Phys Chem A 105:5106.
69. Nir E, Müller M, Grace LI, de Vries MS (2002) Chem Phys Lett 355:59.
70. Onidas D, Markovitsi D, Marguet S, Sharonov A, Gustavsson T (2002) J Phys Chem B 106:11367.
71. Pal SK, Peon J, Zewail AH (2002) Chem Phys Lett 363:363.
72. Peon J, Zewail AH (2001) Chem Phys Lett 348:255.
73. Percourt JML, Peon J, Kohler B (2001) J Am Chem Soc 123:10370.
74. Perun S, Sobolewski AL, Domcke W (2005) Chem Phys 313:107.
75. Perun S, Sobolewski AL, Domcke W (2006) J Phys Chem A 110:13238.
76. Perun S, Sobolewski AL, Domcke W (2006) J Phys Chem A 110:9031.
77. Piuzzi F, Mons M, Dimicoli I, Tardivel B, Zhao Q (2001) Chem Phys 270:205.
78. Plützer C, Nir E, de Vries MS, Kleinermanns K (2001) Phys Chem Chem Phys 3:5466.
79. Schultz T, Samoylova E, Radloff W, Hertel IA, Sobolewski AL, Domcke W (2004) Science 306:1765.
80. Shukla MK, Leszczynski J (2005) J Phys Chem A 109:7775.
81. Shukla MK, Leszczynski J (2005) J Phys Chem B 109:17333.
82. Shukla MK, Mishra SK, Kumar A, Mishra PC (2000) J Comput Chem 21:826.
83. Sobolewski AL, Domcke W (1999) J Phys Chem A 103:4494.
84. Sobolewski AL, Domcke W (2002) Eur Phys J D 20:369.
85. Sobolewski AL, Domcke W (2004) Phys Chem Chem Phys 6:2763.
86. Sobolewski AL, Domcke W, Dedonder-Lardeux C, Jouvet C (2002) Phys Chem Chem Phys 4:1093.
87. Sobolewski AL, Domcke W, Hättig C (2005) Proc Natl Acad Sci USA 102:17903.
88. Sprik M (1998) Faraday Discuss 110:437–445.
89. Sprik M (2000) Chem Phys 258:139.
90. Strickler SJ, Berg RA (1962) J Chem Phys 37:814.
91. Tanner C, Manca C, Leutwyler S (2003) Science 302:1736.
92. Tomić K, Tatchen J, Marian CM (2005) J Phys Chem A 109:8410.
93. Troullier N, Martins JL (1991) Phys Rev B 43:1993.
94. Tully JC (1990) J Chem Phys 93:1061.
95. Tully JC (1998) In: Berne BJ, Ciccotti G, Coker DF (eds) Classical and Quantum Dynamics in Condensed Phase Simulations, World Scientific, Singapore.
96. Tully JC (1998) In: Thompson DL (ed) Modern Methods for Multidimensional Dynamics Computations in Chemistry, World Scientific, Singapore.
97. Tully JC, Preston RK (1971) J Chem Phys 55:562.
98. Ullrich S, Schultz T, Zgierski MZ, Stolow A (2004) Phys Chem Chem Phys 6:2796.
99. Černý J, Špirko V, Mons M, Hobza P, Nachtigallová D (2006) Phys Chem Chem Phys 8:3059.
100. Watson JD, Crick FHC (1953) Nature 171:737.
101. Zewail AH (2000) Angew Chem Int Ed 39:2586–2631.
102. Zgierski MZ, Patchkovskii S, Fujiwara T, Lim EC (2005) J Phys Chem A 109:9384.
103. Zgierski MZ, Patchkovskii S, Lim EC (2005) J Chem Phys 123:081101.